X-811-73-39
PREPRINT

NASA TM X- 70707

DIFFRACTION STUDIES APPLICABLE TO 60-FOOT MICROWAVE RESEARCH FACILITIES

RICHARD F. SCHMIDT

JULY 1973

GSFC

GODDARD SPACE FLIGHT CENTER
GREENBELT, MARYLAND

For information concerning availability
of this document contact:

Technical Information Division, Code 250
Goddard Space Flight Center
Greenbelt, Maryland 20771

(Telephone 301-982-4488)

X-811-73-39

DIFFRACTION STUDIES APPLICABLE TO 60-FOOT MICROWAVE RESEARCH FACILITIES

Richard F. Schmidt

July 1973

GODDARD SPACE FLIGHT CENTER
Greenbelt, Maryland

DIFFRACTION STUDIES APPLICABLE TO 60-FOOT MICROWAVE RESEARCH FACILITIES

Richard F. Schmidt
Network Engineering Division

ABSTRACT

The principal features of this document are the analysis of a large dual-reflector antenna system by vector Kirchhoff theory, the evaluation of subreflector aperture-blocking, determination of the diffraction and blockage effects of a subreflector mounting structure, and an estimate of strut-blockage effects. Most of the computations are for a frequency of 15.3 GHz, and were carried out using the IBM 360/91 and 360/95 systems at Goddard Space Flight Center.

The Fortran IV computer program used to perform the computations is of a general and modular type so that various system parameters such as frequency, eccentricity, diameter, focal-length, etc. can be varied at will. The parameters of the 60-foot NRL Ku-band installation at Waldorf, Maryland, were entered into the program for purposes of this report. Similar calculations could be performed for the NELC installation at La Posta, California, the NASA Wallops Station facility in Virginia, and other antenna systems, by a simple change in IBM control cards. A comparison is made between secondary radiation patterns of the NRL antenna measured by DOD Satellite and those obtained by analytical/numerical methods at a frequency of 7.3 GHz.

CONTENTS

ILLUSTRATIONS

PRECEDING PAGE BLANK NOT FILMED

ILLUSTRATIONS (Continued)

ILLUSTRATIONS (Continued)

GLOSSARY OF NOTATION

Symbol	Meaning
λ	wavelength
cpu	central processor unit
ATS	Applications Technology Satellite
GHz	giga-Hertz
$\bar{E}(x', y', z')$, $\bar{H}(x', y', z')$	scattered electric and magnetic vector fields
x, y, z	Cartesian coordinates
r, θ, ϕ	spherical coordinates
$\bar{n}_1$	unit normal to surface
ψ	Solution to wave equation
$\nabla\psi$	vector gradient of ψ
ds	differential area
μ, ϵ	constitutive parameters: magnetic permeability, inductive capacity
ω	angular frequency
j	imaginary operator = $\sqrt{-1}$
$\bar{e}_i, \bar{h}_i$	electric and magnetic polarization vectors
k	wave number
$\hat{1}_r, \hat{1}_\theta, \hat{1}_\phi$	spherical basis vectors
$\hat{i}, \hat{j}, \hat{k}$	Cartesian basis vectors
F	focal length
γ_i	surface
σ, ζ	radial and angle variables of a cylindrical net
S	source strength
N	exponent of directive source
$\mathcal{F}$	directive point source
$\bar{v}$	polarization moment

Symbol	Meaning
α, β, γ	Euler angles
$\bar{\rho}_\epsilon$	feed displacement vector with components $(x_\epsilon, y_\epsilon, z_\epsilon)$
D	diameter
a, c	parameters of a hyperboloid
LI_1, LI_2	sampling resolution on surfaces γ_1, γ_2 respectively in wavelengths
EOS	Earth Observation Satellite
R, Θ, Φ	spherical coordinates for observing feeds and subsystems
A	area
z_1, z_2	complex numbers
BW	beam width
SLL	side-lobe level
db	decibel
Π_K	reference plane
Δ	increment
f	frequency
ψ	phase (note context)

DIFFRACTION STUDIES APPLICABLE TO 60-FOOT MICROWAVE RESEARCH FACILITIES

INTRODUCTION

The Antenna Systems Branch, Network Engineering Division at Goddard Space Flight Center has developed, and maintains, a general-purpose digital computer program for calculating diffraction patterns of reflector-type antenna systems. A dual-reflector capability was achieved about one year ago to compute both Fresnel and Fraunhofer diffraction patterns in either the transmit or receive mode of operation. The program integrates over charge and current distributions on reflector surfaces in ordinary physical 3-space to produce scattered electric and magnetic field magnitudes, wavefronts, and time-average Poynting vectors, using a complex-vector Kirchhoff approach with Kottler boundary integral, satisfying Maxwell's equations.

Discussions between GSFC, NRL, and NELC personnel indicated that the subject diffraction program was well-suited for providing the following characteristics: directive gain, aperture efficiency, spillover efficiency, diffraction effects from mounting plates, and an estimate of secondary blockage effects due to the hyperboloidal subreflector and the associated support struts for large microwave facilities at K-band. Data on beamwidth, side-lobe levels and cross-polarization components are also provided by the program. A point of concern at the outset of this effort, which included a comparison of computed results with actual measured patterns obtained via DOD Satellite at 7.3 GHz, was the electrical size of the main aperture at 15.3 GHz. The GSFC program had given excellent results for dual-reflector systems with reflectors around 100 λ by 100 λ, and single-reflector systems with reflectors approximately 500 λ by 500 λ, but the present study of the Waldorf antenna, Figure 1, involved an aperture approaching 1000 λ by 1000 λ and was also a dual-reflector configuration.*

Computation of the diffraction patterns of large K-band dual reflector antennas, particularly when appearing in array, had presented a challenge for some time in TDRSS studies. The analysis of the 60-foot NASA/NRL/NELC microwave installations was, therefore, undertaken to determine whether or not it was feasible to obtain meaningful results for such a problem with the existing integration algorithm. Annexation of the strut-blockage subroutine via a Babinet's principle was an added complication that had received only limited verification at the outset of this study. The composite subreflector posed no difficulty as this capability

---

*The NRL Waldorf installation was funded by NASA to collect ATS-5 rainstorm data at 15 GHz.

had been tested extensively several years earlier. Some modification of the basic program was anticipated — and required — due to the inevitable trade-off between computer cpu-time and accuracy. Computer program development is usually determined by actual requirements and applications, and in this instance direct benefits were realized for EOS 3-reflector passive multichannel microwave radiometer (PMMR) antenna computations, ATS-F diffraction studies, STDN 40-foot and 85-foot antenna analyses, and TDRSS trade-off studies for determination of the antenna payload.

FORMULATION OF THE SCATTERED FIELDS

In the transient mode of operation the fields due to the main or parabolic reflector (γ_2) of the system are obtained from

$$\bar{E}(x', y', z') = \frac{1}{j\omega\epsilon}\,\frac{1}{4\pi}\int_{\gamma_2}\left[(\bar{n}\times\bar{H}_2)\cdot\nabla\right]\nabla\psi\, ds - j\omega\mu\,\frac{1}{4\pi}\int_{\gamma_2}(\bar{n}_2\times\bar{H}_2)\,\psi\, ds,$$

$$\bar{H}(x', y', z') = -\frac{1}{4\pi}\int_{\gamma_2}(\bar{n}_2\times\bar{H}_2)\times\nabla\psi\, ds,$$

where

$$\psi = \frac{e^{-jkr}}{r}$$

and

$$\nabla\psi = -\left(jk + \frac{1}{r}\right)\psi\,\hat{1}_r,$$

taking $\hat{1}_r$ in a local context on the reflecting surface.

Since only the magnetic field $\bar{H}_2$ is required on γ_2, the integral

$$\bar{H}_2(x_2', y_2', z_2') = -\frac{1}{4\pi}\int_{\gamma_1}(\bar{n}_1\times\bar{H}_1)\times\nabla\psi\, ds$$

over the hyperbolic subreflector (γ_1) is sufficient to obtain the illumination of γ_2 due to γ_1. The subsystem surface may be extended to include the flat mounting plate (γ_1').

The preceding formulation is applicable in both far-field (Fraunhofer) regions and intermediate near-field (Fresnel) regions, and is well-suited to dual or multiple-reflector systems, where a point on one surface may lie in the Fresnel region of another surface over which an illumination distribution is being integrated. It can be shown that the formulation used here is identical to the Kirchhoff-Kottler and Franz formulations, but is better-suited to numerical integration methods than the latter.*

GEOMETRY

The geometry for the problem is shown in a photograph designated Figure 1. Input parameters and surface equations are as follows.

Paraboloid (γ_2)

$$x = \sigma \sin \zeta, \qquad y = -\sigma \cos \zeta, \qquad z = \frac{\sigma^2}{4F} + z_{1P}$$

$z_{1P} = -F = -18.0'$

$\sigma_{max} = 30.0'$

$\sigma_0 = 0.0'$ (initially, without obscuration)

Hyperboloid (γ_1)

$$x = \sigma \sin \zeta, \qquad y = -\sigma \cos \zeta, \qquad z = c\,(1 + \sigma^2/a^2)^{1/2} + z_{1H}$$

$z_{1H} = -c\epsilon = -5.87'$

$a = 4.03'$

$c = 4.27'$

---

*See Ref. 1, 2, 3, and 4.

$\sigma_{max} = 3.00'$

$\sigma_0 = 0.0'$

Mounting Plate (γ_1')

$$x = \sigma \sin \zeta, \qquad y = -\sigma \cos \zeta, \qquad z = c_c \sigma + z_{1c}$$

$z_{1c} = 0.0'$

$c_c = 0.0$

$\sigma_0 = 3.00'$

$\sigma_{max} = 4.41'$

Feed $(\mathcal{F})$

$\mathcal{F} = S \cos^N \Theta \Rightarrow$ directive field

$S = 1.0 \Rightarrow$ source strength

$N = 33.2 \Rightarrow$ approximately -10 db edge taper on γ_1

$P(I) = 1.0,\ P(J) = P(K) = 0.0 \Rightarrow$ polarization moments

$\alpha = \beta = \gamma = 0.0^\circ \Rightarrow$ Euler angles for feed

$x_\epsilon = y_\epsilon = 0.0',\ z_\epsilon = -2c\epsilon = -11.7' \Rightarrow$ feed location

$F/D = 0.30 \Rightarrow$ F - number of paraboloid

The subroutines for the paraboloid and the hyperboloid require no elaboration, however, the subroutine for the flat mounting plate deserves a word of explanation. In the physical installation the plate is flat and is situated in the focal-plane of the paraboloid. From the point of view of the simulation, the electromagnetic scattering from the plate is due to that portion of the plate which is not shielded from the feed by the hyperboloid. The plate can therefore be thought of as having a central hole of radius $\sigma = 3.00'$, the radius of the hyperboloid.

Although the plate is square, 93.46 inches along an edge, the equivalent area of a flat circular disc was used to compute the effects of the mounting plate. To be more precise, the annulus of a flat circular disc was used in the simulation. This permitted the utilization of an existing subroutine (cone) which exhibited rotational symmetry. All integration over γ_1 and γ_1' was then done by means of a cylindrical (σ, ζ) net, and a Cartesian (x, y) net for the square plate was avoided. The parameter c_c is the inverse-slope of a cone; the latter degenerates into a flat disc when c_c vanishes. Choosing $z_{1c} = 0.0'$ situates the flat disc in the focal plane.

RESULTS OF THE "LITERAL" METHOD

Under ray optics, an ordinary Cassegrain system constitutes a one-to-one mapping from the subreflector onto main reflector. Under diffraction, the illumination of the main reflector is obtained from a many-to-one mapping of the illumination distribution (charge and current) of the subreflector onto the main reflector. This many-to-one mapping has been termed the "literal" method since it is the natural result of redundantly applying the Huygens principle to multiple-reflector systems. The reader may wish to assess the awkwardness of this approach when three or more surfaces make up the system.*

Since application of the "literal" method was expected to result in excessive cpu-time and core requirements for a dual-reflector system in which the main reflector exceeded 800 λ by 800 λ; an approach which regarded the prime-feed/subreflector combination as an effective "equivalent source" was favored. Figure 2 shows the far-field pattern via the "literal" method for this Cassagrain system without mounting-plate, central obscuration, or strut obscuration at a frequency of 1.53 GHz. Results appear acceptable out to 3 degrees in the theta domain for this low-frequency test case obtained at a sampling of $LI_1 = 0.25$ and $LI_2 = 2.5$ on the subreflector and main reflector respectively. The far-field pattern at 15.3 GHz was also obtained via the "literal" method, using the same input parameters as before, and is shown as Figure 3. This result was obtained for $LI_1 = 1.25$ and $LI_2 = 6.00$, storing the illumination values on γ_1 and γ_2, and taking advantage of the biplanar symmetry that exists for the problem with respect to illumination on the reflector surfaces. Results appear credible out to 0.3 degrees in the theta domain although null-filling is in evidence at N_4. (Null-filling is not certain at N_2 since $\Delta\theta = 0.005$ degree does not resolve a good minimum or true null unambiguously.) Considering that a ten-fold increase in frequency occurred between Figure 2 and Figure 3, the side-lobe structure out to 0.3 degrees corresponds to 3.0 degrees of the previous computation. The onset

---

*A three-reflector "telescope" system was studied for the Earth Observation Satellite (EOS), however, the "literal" method was avoided due to prohibitive cpu-times involved.

of failure of the solutions due to inadequate integration sampling (LI_1, LI_2) is apparent from the null-filling, anomalous null-to-null sidelobe angular width, sidelobe level, and departure of side-lobe peaks from an asymptote or monotonic law of descent. It can be seen from Figure 2 and Figure 3 that degradation sets in progressively for larger values of theta (θ).

Since the practical limits of cpu time and core had already been exceeded in obtaining results at 15.3 GHz, Figure 3, and since the effects of the flat mounting plate and struts had not yet been included, the "literal" method was abandoned for the remainder of this particular study. The "equivalent source" method which derives scattered field data from the prime-feed subreflector combination was adopted, and even this approach was found to be demanding with respect to cpu-time and core when the effects of the mounting plate were included. The annular area of the mounting plate was found to be about equal to that of the hyperboloid. Integration sampling intervals somewhat greater than those prescribed by the antenna analogue to Shannon's sampling theorem* were finally used, but this precedes the development.

SUBSYSTEM PATTERNS

The "equivalent source" method is now detailed without inclusion of the annular mounting plate to illustrate some of the problems and show the reader the basis for the sampling (LI_1) on the subreflector (γ_1). First of all, there is the question of the range (R) at which field values scattered by the prime-feed/subreflector combination should be reevaluated. See the expression for $\overline{H}_2(x_2', y_2', z_2')$. Clearly, the values on a parabolic locus (γ_2) are ultimately required, but this view obscures the fact that the prime-feed/hyperboloid subsystem behaves as a virtual spherical point-source at F. A large value of R, to simulate infinite range, has some merit. It is possible, however, that in general there may be near-field considerations since any point on γ_2, at 15.3 GHz, is in the intermediate near-field of γ_1 if the physical dimensions of the latter are regarded. Another viewpoint is that the effective diameter for a hyperboloid fed at the conjugate focal point is not anything like the physical diameter, but is essentially zero (i.e. a point source) in $R = 2d^2/\lambda$, the usual criterion for discerning "near-field" and "far-field".

The range (R) was initially chosen equal to the focal distance (F) of the paraboloid for the "equivalent source" method since this allows one to observe the purity of the wavefront on a circular arc whose center is the phase center of the prime-feed/hyperboloid subsystem being studied. This is especially convenient because

---

*Ref. 5, page 321.

the nearly constant phase on this spherical arc (R = F) can now be used to further develop the "equivalent source" method. Both field phase and amplitude on this arc are placed in core for a preselected resolution in theta ($\Delta\theta = 2°$) between the vertex of γ_2 and the geometrical bound or edge of γ_2. This "equivalent source" data is then modified by the factor $e^{-jk\rho}/\rho$ which effectively provides for the differential phase between the vertex wavefront (R = F) and the paraboloid (γ_2) as well as the space divergence of the amplitude of the illumination arriving at γ_2. This is in lieu of computing the difference between the arc R = F and ρ to the paraboloid for each differential (incremental) area.

The absolute phase of the source has then been changed in the amount e^{-jkF} and the original source strength has been multiplied by 1/ F, both of which are <u>irrelevant</u> with regard to the final diffraction pattern. This can be seen as follows.

Assume a virtual point source of strength S_0, initial phase ψ_0, and directivity $\mathcal{F}$ such that

$$\left[(S_0\, e^{j\psi_0}\, \mathcal{F})\ \frac{e^{-jk\rho}}{\rho}\right] = \left[(S_0\, e^{j\psi_0}\, \mathcal{F})\ \frac{e^{-jkF}}{F}\right] T,$$

spherical wave expanded out to γ_2 | spherical wave expanded out to R = F

where T is the transformation which rigorously preserves both field phase and amplitude in going from the arc R = F to the reflector γ_2.

$$T = \left(\frac{e^{-jk\rho}}{\rho}\right)\ (F\, e^{+jkF})$$

Now the first factor of T was used, as stated previously, but the second factor was ignored (i.e., read-in "unity"). Failure to include the second factor therefore multiplies the assumed source by the reciprocal of that factor:

$$[S_0\, e^{j\psi_0}\, \mathcal{F}]\ \left[\frac{e^{-jkF}}{F}\right]$$

so that the omission results in nothing more than a reinterpretation of the real source as

$$\left[\left(\frac{S_0}{F}\right) e^{j(\psi_0 - kF)} \mathcal{F}\right]$$

In other words, amplitude and initial phase of the assumed source have been modified in an irrelevant manner. The validity of the preceding discussion is further borne out by a comparison of the secondary radiation patterns by the "literal" method with those of the "equivalent-source" method using the prime-feed/hyperboloid subsystem. Obviously, the approach is predicated on a spherical law of divergence between the arc $R = F$ and the value ρ on the main reflector (γ_2).

Figure 4 shows the (relative) phase and amplitude of the totality of the Huygens wavelets scattered from the hyperboloid (γ_1) onto the spherical arc ($R = F = 18'$) passing through the vertex of γ_2, for a sampling interval of $LI_1 = 1.25$. Note the geometrical bound of γ_2. The result is extremely coarse, however, surprisingly good secondary patterns can sometimes be obtained from the main reflector with such an "equivalent source". Phase dominates problems of this type, and rather large amplitude variations are a lesser consideration. In Figure 4 the phase excursions approach ±180 degrees, and it is remarkable that good results can be obtained for such departure from a pure spherical wavefront.

Figure 5 shows the (relative) phase and amplitude of the scattered electric field on $R = F = 18'$ as for Figure 4, but $LI_1 = 0.600$. It can be seen that the large "spike" in amplitude has diminished near $\Theta = 180°$, and the variations, generally, are smaller. More importantly, the phase has become constant to within ±20 degrees or so for $100° \leq \Theta \leq 140°$, which represents considerable energy in an annular region of the sphere $R = F = 18'$. The phase variations still approach ±180 degrees in the domain $140° \leq \Theta \leq 180°$. Also note the behavior of the phase plot outside of the geometrical bound $90° \leq \Theta \leq 100°$. It is still violently oscillatory, but less so than in the preceding instance.

Figure 6 shows the (relative) phase and amplitude of the scattered field in $R = F = 18'$ for $LI_1 = 0.300$, the sampling used in most subsequent dual-reflector computations. The improvement over Figure 5 is striking. Both phase and amplitude closely approach the classical ray optics concept for scattering by the subsystem. Over the domain of interest, $100° \leq \Theta \leq 180°$, the amplitude is a monotonically decreasing function with a ripple of approximately ±1 db, while the phase plot or wavefront exhibits a variation of about ±10 degrees. The scattered values of Figure 6 were considered "stable" solutions with respect to the integration sampling (LI_1). Once stored, these values are not computed again even though main reflector obscuration by the hyperboloid and/or the struts is considered subsequently. None of these values are computed anew for different secondary pattern cuts $\phi = 0°$, $\phi = 45°$, $\phi = 90°$, etc.

Figure 7 shows the subsystem phase and amplitude pattern at R = F = 18' with the flat annular mounting plate included. The reader will notice that the hyperboloidal part of the subsystem was sampled at $LI_1 = 0.300$, but the flat annular mounting plate was sampled at $LI_1' = 1.00$ in carrying out the integration process. It was determined by means of separate calculations with the program that the differences between $LI_1' = 0.500$ and $LI_1' = 1.00$ were negligible, therefore, the coarser interval was selected in forming this subsystem pattern in the interest of cpu-time reduction.

The phase and amplitude of the backscattered fields in Figure 7 are perturbed by the influence of the flat annular disc.* In the region $100° \leq \Theta \leq 160°$, which is between the geometrical bounds of γ_1 and γ_2, the amplitude exhibits a normal monotonic descent over most of the area of interest. The exception is the interval $140° \leq \Theta \leq 166°$. The phase is constant, as required, to within ±15 electrical degrees or so over most of the region of interest, however, it varies ±50 electrical degrees in the excepted interval. Confining the discussion to the interval $100° \leq \Theta \leq 166°$ between the geometrical bounds, and regarding areas on a unit sphere through which power is flowing, the percentage of perturbed to unperturbed power is estimated (without respect to power density variations) by areas alone.

$$A = \iint ds = \iint R^2 \sin\Theta \, d\Theta \, d\Phi = -2\pi \cos\Theta \Big|_{\Theta_1}^{\Theta_2}$$

$$A_{TOTAL} = -2\pi(\cos 166° - \cos 100°)$$

$$A_{PERTURBED} = -2\pi(\cos 166° - \cos 140°)$$

$$\frac{A_{TOTAL}}{A_{PERTURBED}} \times 100 \cong 25\%$$

---

*See Appendix B.

It is anticipated, therefore, that the Kirchhoff integration over the illumination distribution on γ_2, using Figure 7 data, will not greatly affect the far-field radiation pattern.

The polarization of the "equivalent source" enters the problem when the integral $\bar{H}_2(x_2', y_2', z_2')$ is evaluated at R = F. It should be noted that the field quantities are complex-vectors due to the unit polarization vectors ($\bar{h}_1$) of the real or physical source. Let the components of the source polarization moment (designated P(I), P(J), P(K) in the program input) be $(v_x, v_y, v_z) = \bar{v}$. Then the magnetic polarization vector incident or γ_1 is

$$\bar{h}_1 = \frac{\bar{\rho} \times \bar{v}}{|\bar{\rho} \times \bar{v}|}$$

and the electric polarization vector is

$$\bar{e}_1 = \frac{\bar{\rho} \times (\bar{v} \times \bar{\rho})}{|\bar{\rho} \times (\bar{v} \times \bar{\rho})|}$$

Only $\bar{h}_1$ is required in the present computations, although $\bar{e}_1$ is probably more familiar and more easily visualized, since only incident magnetic fields $\bar{H}_1 = |\bar{H}_1| \bar{h}_1$ appear in the diffraction integral

$$\bar{H}_2(x_2', y_2', z_2') = -\frac{1}{4\pi}\int_{\gamma_1} (\bar{n}_1 \times \bar{H}_1) \times \nabla\psi \, ds$$

at R = F.

The "equivalent source" method is relatively straightforward, with one possible exception. It has been shown that the backscattered illumination is a set of complex-vectors, and the vector character of the problem enters via the unit polarization vector ($\bar{h}_1$). The complex character of the problem is associated with the time domain or phase of the fields at various points. Although the present computations were not affected, a delicate question arises concerning intermediate complex values for analogue data. For example, the E-plane, H-plane eccentricity of the backscattered fields were disregarded here, and the spherical cut $(r, \theta, \phi) = (18', \theta, 0°)$ provided phase and amplitude data for all other cuts via a trivial interpolation between $\phi = 0°$ and $\phi = 360°$. Suppose the pattern eccentricity had been large. Additional cuts at $\Delta\phi = 45°$ or $\Delta\phi = 15°$, etc. could have been employed to display the character of the backscattered fields. This would have raised the following question.

What is the "average" of two complex numbers (ordered pairs)? How does one interpolate or find an intermediate complex number between two given complex values? One approach might be to take the average of the magnitudes and the average of the arguments or phase angles. Another approach might be to average the real and imaginary parts separately to produce an intermediate value. Unfortunately, the two approaches lead to different results for an arbitrary choice of "nearly equal" complex numbers: z_1, z_2. Both methods can be very disappointing from a practical point of view, not to mention the rigorous point of view. It is possible to obtain such interesting results as an argument or phase which is approximately π radians different from the argument of z_1 and z_2. Also, it is possible to obtain an amplitude which is either literally zero or approximately zero even though the magnitudes of z_1, z_2 were arbitrarily large! An area of difficulty has been identified here, however, the impact on the present problem is negligible. Many "cuts" on analogue data relieve the severity of the problem as do a nearly spherical wavefront and small E-plane, H-plane eccentricity.

RESULTS OF THE "EQUIVALENT SOURCE" METHOD

The reference pattern, in the following sequence of 15.3 GHz far-field radiation patterns from the dual-reflector system, is Figure 8. As stated previously, subreflector sampling was stable at $LI_1 = 0.300$. It was found that main reflector sampling was stable at $LI_2 = 6.00$ if the first three or four sidelobes only were required for study.* Beamwidth (BW) equals approximately .070 degree, and the first sidelobe level (SLL_1) is approximately -25.5 db below the beam maximum.

The first departure from the reference pattern is Figure 9, which shows the effect of central obscuration due to the hyperboloid ($\sigma_0 = 0.0'$, $\sigma_{max} = 3.0'$). The range of integration over γ_2 is now restricted by $\sigma_0 = 3.0'$, $\sigma_{max} = 30.0'$. A weak interferometer effect is anticipated and observed. (BW $\approx$ .070 degree, $SLL_1 \approx -23.0$ db.) A discussion of directive gain degradation is deferred to a summary at the end of this section.

---

*Grating lobes of classical array theory do not appear due to the spatial distribution of the LI samples on the polar (σ, ζ) net.

The second departure from the reference pattern is Figure 10, and shows the effect of central obscuration due to the hyperboloid and the flat mounting plate bounded by $\sigma_0 = 0.0'$, $\sigma_{max} = 4.41'$. The range of integration over γ_2 is now restricted by $\sigma_0 = 4.41'$, $\sigma_{max} = 30.0'$. In this calculation the backscattering from the annular mounting plate is also included. Recall Figure 7. It can be seen that beamwidth is negligibly affected relative to the preceding Figure 9, but the sidelobe structure has been altered significantly. ($SLL_1 \approx - 19.5$ db.)

The third departure from the reference pattern is Figure 11, and is the "complete" simulation of the physical structure for this report. Hyperboloid and mounting plate obscuration as well as scattering are present as for Figure 10, but strut blockage has now been taken into account. Beamwidth is not altered significantly, and has narrowed slightly, if anything. Sidelobe structure has taken on some unusual characteristics. Pattern level changes are not very large. ($SLL_1 \approx - 19.2$ db.) The $\phi = 90°$ cut, not shown, closely resembled the $\phi = 0°$ cut of Figure 11 in all except the fine detail. A $\phi = 45°$ cut, also not shown, exhibited relatively high sidelobes ($SLL_1 \approx - 17.5$ db).

The level of the electric field E_θ (main polarization) for the preceding calculations, Figure 8 through 11, as derived from the Kirchhoff integration compare as follows.

Figure 8	reference pattern	- 94.529 db
Figure 9	hyperboloid obscuration included	- 94.683 db
Figure 10	hyperboloid and mounting-plate obscuring and scattering	- 94.726 db
Figure 11	complete system with (secondary) strut blockage	- 95.030 db

The implication of these values is that elements of the system degrade the gain approximately as shown below.

hyperboloid obscuration	0.15 db
mounting-plate effects	0.04 db
spar obscuration	0.30 db

It appears that the combined gain degradation is about 0.5 db and the mounting plate, though comparable in area with the hyperboloid, has a negligible influence. Details of the development leading to the obscuration estimates can be found in the Appendix A of this report. Cross polarization components are a natural by-product with the GSFC diffraction program since the vector integration in Cartesian coordinates leads to fields which are simply projected onto the spherical basis vectors to produce main and cross-polarization components at the close of the calculations. None of the cross-polarization data are presented here as no degradation problem was noted in this characteristic of the system.

The preceding results demonstrated that the existing GSFC diffraction program was capable of dealing with large dual-reflector Ku-band antenna systems. A credible beam solution was obtained for the 60-foot Cassegrain installation and such considerations as cpu-time, core-requirements, significant digits, accuracy, etc. did not individually or collectively present any insurmountable problems. In a sense, the body of this report represented a first milestone. A secondary objective was the correlation of the computed results with a good Ku-band field measurement for precisely the same system that had been simulated. This objective was not realized since reliable 15.3 GHz data for these sites did not become available, even though considerable interest existed concerning the shape of a Ku-band pattern that was influenced by subsystem obscurations, a large mounting-plate, and strut blockage. Measured field-pattern data did become available at a lower frequency, however, and it was decided to simulate this configuration also by means of the diffraction program to obtain at least one comparison between the analytical/numerical approach and field practice.

The low-frequency (C-band) comparison is detailed in Appendix B of this report. It was determined that certain deficiencies existed in the initial analysis when the mounting-plate was included, but only the far-out sidelobes were significantly affected. Appendix B also includes the results of a 15.3 GHz simulation using the improved analysis.

SUMMARY

This report has attempted to illustrate some of the practical problems and solutions for a dual-reflector geometry that was complicated by a compound subreflector, a central aperture obscuration, and strut blockage of the main aperture. Perhaps the outstanding obstacle was that the paraboloidal reflector dimensions for this Cassegrain system, in wavelengths, precluded utilization of the "literal" method of Huygens under a Kirchhoff-Kottler type of formulation. A fundamental difficulty concerning the interpolation of complex numbers was encountered. In addition, it was shown that expansion of wavefronts from a spherical locus cannot proceed by means of a single, simple spherical divergence rule when multiple phase-centers are encountered. The degradation of results in such cases will depend on the location and weight of those phase centers. An estimate of strut blockage effects was included, and this was based on a simple Babinet principle which deleted umbral regions for the Kirchhoff integration. It was noted that shadow updating is not required when the sidelobe structure of interest lies in a

small angular region away from the system axis. Primary blockage, as viewed from the virtual origins of the subsystem, was not considered. Mutual coupling effects were, likewise, not considered.

The subjects of system gain and directive gain were not covered comprehensively since the principal objective was the computation of pattern shape or form. Obviously the application of the definition of directive gain

$$G_D = \frac{P(\theta, \phi)}{\frac{1}{4\pi} \iint P(\theta, \phi) \sin\theta \, d\theta \, d\phi}$$

over the half-space containing the radiation pattern of this system would be extremely costly in cpu-time. A comparison method, based on the notion of a degenerate paraboloid ($F = \infty$) of identical diameter and uniform phase, amplitude, and polarization illumination might be employed successfully here. An estimate of gain degradation due to hyperboloid obscuration, mounting-plate effects, and span obscuration was included. A linear polarization state was assumed throughout for convenience.

The 7.3 GHz satellite data for the Waldorf, Maryland installation, as furnished by the U.S. Naval Research Laboratory, greatly stimulated interest in the simulation. A valuable comparison between "theory" and "practice" lead to the exploration of several methods for computing the diffraction patterns. All approaches used here simulated the main beam and first sidelobe level fairly well. Significant differences between methods lay in the far-out sidelobe region. Techniques evolved in this study are being applied to diffraction problems for ATS-F, STDN, EOS, and TDRSS.

Diffraction studies are being continued, however, the investigation of the present configuration is terminated. This is an interim report.

ACKNOWLEDGMENTS

The author is indebted to the existing technical literature, and to R. Miezis and W. Bartley (Programming Methods, Inc.) for the dual-reflector program used in these calculations. In addition, the author is indebted to R. A. Lefande of the U.S. Naval Research Laboratory, Washington, D.C., for useful technical discussions, satellite and other data, and a guided visit to the Waldorf installation.* A

---

*Reference 7 was also supplied for background purposes.

discussion of the simulation with Mr. C. A. Bass of the Naval Electronics Laboratory, San Diego, California is also acknowledged.

REFERENCES

1. Stratton, J. A., "Electromagnetic Theory," McGraw-Hill Book Company, Inc., 1941

2. Schmidt, R. F., "The Calculation of Electromagnetic Fields by the Kirchhoff-Kottler Method," X-525-70-293, Goddard Space Flight Center

3. Schmidt, R. F., "The Calculation of Electromagnetic Fields in the Fresnel and Fraunhofer Regions using Numerical Integration Methods," X-811-71-392, Goddard Space Flight Center

4. Franz, W., "Zur Formulierung des Huygensschen Prinzips," Z. Naturforschg., Vol. 3a, July 1948

5. Skolnik, M. I., "Introduction to Radar Systems," McGraw-Hill Book Company, Inc., 1962

6. Kaplan, W., "Advanced Calculus," Addison-Wesley Publishing Company, Inc., 1959

7. Bass, C. A. and Townsend, D. H., "The NRL Microwave Space Research Facility," NRL Report 6921, August 11, 1969

APPENDIX A

SECONDARY BLOCKAGE CALCULATIONS

Figure 12 depicts a general secondary blockage or obscuration example O_2. For high-gain, small beamwidth problems the interesting features of the radiation pattern do not lie far from $\theta = 0°$ in the θ-domain, and the square blockage area can be taken as O_1 without serious error. An accurate projection of the support trusses is not attempted in Figure 12 which illustrates only the general nature of the problem and its solution. The obscuration O_1 can be taken to represent the hyperboloid and square mounting plate encountered earlier in this report. In evaluating the Kirchhoff-Kottler class diffraction integral over γ_2 it is sufficient, for a first-order estimate of blockage effects based on a Babinet's principle, to delete the area O_1 in the integration for the scattered field.

$$\bar{E}(x', y', z') = \frac{1}{j\omega\epsilon}\,\frac{1}{4\pi}\int_{\gamma_2 - O_1}\left[(\bar{n}_2 \times \bar{H}_2)\cdot\nabla\right]\nabla\psi\, ds - j\omega\mu\,\frac{1}{4\pi}\int_{\gamma_2 - O_1}(\bar{n}_2 \times \bar{H}_2)\,\psi\, ds$$

In cases where lower-gain, larger-beamwidth problems are encountered, the same Babinet's approach requires an up-dating of the shadow for every observer position $(\infty, \theta, \phi) = (R, \theta, \phi)$. Figure 12 illustrates how the physical obstacle has a new "shadow" or umbral region on γ_2 for every $\theta \neq 0$. A convenient method of dealing with this situation, which is complicated by the fact that the integration for $\bar{E}(x', y', z')$ is actually taken on the surface γ_2 and the shadow contours may be quite general in any practical case, is to introduce a reference plane (Π_K).[1]

For a given observer position (∞, θ, ϕ), the area to be deleted from the integration (O_2) is identified on γ_2 by its boundary contour (C_2). These points can be projected into the reference plane (Π_K) to form O_2'. Where a large number of obscurations are present this method is especially convenient, since all deletions can be accomplished by means of a Cartesian net on Π_K. The true area deleted on γ_2 is related very simply to the projected area in Π_K via[1]

$$\Delta S = \sec\gamma^*\,\Delta A$$

(increment of area on γ_2) (increment of area on Π_K)

---

[1] Reference 6, p. 208.

where the angle γ^* is obtained from the dot product between the unit normal ($\bar{n}_2$) to the surface γ_2 and the basis vector $\hat{k}$.

$$\cos \gamma^* = \bar{n}_2 \cdot \hat{k}$$

It is also possible to employ curve-fitting to the contour C_2' on Π_K in the determination of ΔA.

The preceding ideas were used in the present report to estimate the effects of main reflector secondary obscuration by the hyperboloidal subreflector, the flat mounting plate, and the 14-inch diameter trusses. Primary obscuration was not included at this stage of the development. Multiple scattering was also ignored. Methods of estimating current distributions on support trusses, and computing the scattered fields of members whose dimensions in terms of a wavelengths are sometimes small, have been considered, but not implemented. Since the directive gain for the antenna was very high, and the beamwidth very small, all of the sidelobe structure of interest was observed for $0° \leq \theta \leq 0.50°$ at 15.3 GHz and $0° \leq \theta \leq 0.80°$ at 7.3 GHz. The obscurations or "shadows" due to subsystem and support struts were therefore not updated with observer angle.

APPENDIX B

A COMPARISON OF MEASURED DATA WITH ANALYTICAL RESULTS

At the conclusion of the series of 15.3 GHz computations contained in the body of this report it was determined that only 7.3 GHz radiation-pattern data would be available for this analysis. Only the "complete" configuration which included mounting plate, subsystem obscuration, and strut blockage effects was recomputed at 7.3 GHz. The results were compared with measured data, $\phi = 0°$ cut, obtained via DOD Satellite Number 16. Figure 13 shows the measured data, provided by the U.S. Naval Research Laboratory. An undetermined amount of noise can be seen for signal levels approximately 20 db below the beam maximum.

Since reduction of the simulation frequency from 15.3 GHz to 7.3 GHz eased the core and cpu requirements significantly, a valuable re-evaluation of the techniques used in the body of the report could be made. Two obvious areas of exploration were considered. First, a study of the effects of interpolation of the backscattered fields from the subsystem composed of a hyperboloidal cap and a flat mounting plate was made. The theta (θ) increment used in Figures 4 through 7 was $\Delta\theta = 0.2$ degrees implying approximately 40 data points in the domain of interest ($100° \leq \theta \leq 180°$). For a sampling criteria of $LI_2 = 3.0$, however, at a wavelength of 0.06431' (15.3 GHz) the amount of data required along a 30-foot parabolic arc is approximately 300 points. Ordinarily this poses no special problem when the subsystem behaves as a virtual point source. Introduction of the flat annular mounting plate perturbed the spherical wavefront, see Figure 7, therefore the required interpolation of field data is no longer empty.

Second, a study of the assumption that the backscattered data from the hyperboloidal cap and flat annular mounting plate could be computed on the arc $R = F$, and then expanded as a spherical wave up to the paraboloidal surface, was undertaken. As mentioned previously, there is some justification for attempting to observe the subsystem fields on a circular arc. The spherical wavefront, or slight departures from it, can be displayed. A decision can then be made relative to the subsystem sampling (LI_1). Furthermore, a parallel experimental effort would logically utilize a circular arc such as $R = F$ to probe the subsystem fields. If ray optics is used to identify the virtual origin of the subsystem fields, see Figure 14, the conclusion is that the hyperboloidal cap has a unique phase center situated at the focal point F, but the flat annular mounting plate has a unique phase center a distance $Z = \overline{FF^*}$ from the focal point. These phase centers have, in general, different amplitude weighting-factors and initial phases associated with them.

In view of the preceding, the expansion of the subsystem fields according to a spherical law, with phase center at focal-point F, is difficult to justify. Since one does not a priori know the location and weight of the various phase centers and expansion about multiple phase centers would be tedious, requiring eventual superposition at the paraboloid, it seemed expedient to compute the subsystem backscattered fields directly on the parabolic locus of the main reflector via diffraction theory. A parallel experimental effort should also proceed along the parabolic law which is to be illuminated, an undesirable complication which would require a separate measurement dependent on each paraboloidal F/D ratio to be employed.

In order to identify the variations introduced by the alternative methods of computing the backscattered phase and amplitude of the fields from the compound subsystem, the 7.3 GHz computations were first done with interpolation on a spherical arc (R = F). The amount of data in the domain of interest ($100° \leq \theta \leq 180°$) was approximately 40 points. The amount of data required on the 30-foot parabolic arc for $\lambda = 0.13'$ (7.3 GHz) is approximately 100 with LI_2 set at 3.0 for Kirchhoff integration. It can be seen that the interpolation is still significant but less critical than at 15.3 GHz. See Figure 15. Four vertical lines on Figure 15 represent the geometrical bounds of the problem. The two outer bounds are the edge of the main reflector and the obscuration due to the subreflector, while the inner bounds show the extremes of the rays originating at the mounting plate under a ray-optics analysis. Figure 16 presents the far-field pattern for the complete Cassegrain system. This result exhibits a monotonic descent in the sidelobe structure which is not seen in the measured data. Due to the presence of noise in the measured pattern, the absolute signal level beyond the first sidelobe is open to question.

At this point the 7.3 GHz calculations were repeated, but without interpolation of the backscattered-field data. A spherical locus (R = F) was retained for these computations. Figure 17 shows the subsystem pattern by this approach. Each of 64 field values was obtained at a spherical angle (θ) pre-computed by means of a separate driver program to correspond to the (σ, ζ) net $LI_2 = 3.0$ criterion on the main reflector arc. Figure 17 should now be compared with Figure 15. The domain of interest was contracted to $100° \leq \theta \leq 166°$ to conserve cpu time since the values outside of the extreme geometric bounds do not enter into the Kirchhoff integration. Significant differences appear between Figure 17 and Figure 15 due to avoidance of the interpolation process which was previously routinely carried out using E_θ and ψ_{E_θ} analogue subsystem backscattered data from the GSFC program.

The far-field pattern corresponding to Figure 17 is Figure 18, and should be compared with Figure 16. Evidently the avoidance of interpolation has improved the quality of the result since the sidelobe envelope is no longer monotonically decreasing, but reproduces the prominent lobe whose peak lies in the vicinity of θ = 0.5 degrees in the measured pattern. It is unfortunate that the measured pattern of Figure 13 contained enough noise to mask nulls and raise sidelobe levels at the -25 db to -30 db level relative to the beam maximum.

Next a parabolic locus, the arc of the main reflector, was used to compute the backscattered subsystem fields at 7.3 GHz. Interpolation was avoided as in the preceding case. Figure 19 shows the field amplitude arriving at the surface of the paraboloid prior to conversion to charge distribution and electric sheet current. The associated phase is not shown since phase varies rapidly on the parabolic arc and order is difficult to recognize with the inclusion of the effects of the flat annular plate. The corresponding far field pattern is Figure 20 and shows considerable departure from Figure 18 and Figure 16. Most interesting, perhaps, is the fact that Figure 20, the best estimate of the far-field pattern obtained with the diffraction program at 7.3 GHz, reproduces a first sidelobe peak at θ = 0.24 degree and a second sidelobe peak at θ = 0.49 degree as in the measured result, Figure 13. The level of the first sidelobe via the program is -20.5 db, and is in exact agreement with measured results. The level of the second sidelobe was computed as -27 db, and a meaningful quantitative comparison at this level cannot be made since noise has spoiled the measured pattern beyond 0.30 degree as evidenced by obliteration of nulls beyond this value of theta. It is noted that the computed result, Figure 20, predicts substantial null-filling around θ = 0.375' degree due to the combined effects of the annular plate subsystem obscuration and strut blockage.

A review of the three approaches used to obtain the 7.3 GHz diffraction pattern forces the conclusion that the parabolic locus approach without interpolation of the backscattered subsystem fields is the better approach. This is particularly true when there is a large departure from the virtual point-source that emanates an ideal set of spherical wavefronts. The favored approach is also the most demanding in terms of cpu time and core requirements. A comparison of computed data with several USNRL patterns obtained by satellite at 7.3 GHz, although in the presence of noise interference, indicated that the spherical-wave expansion assumption and subsystem data interpolation were responsible for significant inaccuracy beyond the main beam and first sidelobe computation. The evidence appeared convincing enough to warrant a re-examination of the 15.3 GHz problem for the "complete" configuration.

Since Figure 7 and Figure 11 in the body of this report present the backscattered subsystem pattern on a spherical locus using interpolation and the corresponding far-field pattern, respectively, the interpolation was avoided in a subsequent study. This produced Figure 21 for the subsystem and Figure 22 for the far-field patterns. It is noted that although the hyperboloidal cap is confocal with the paraboloid and all rays incident upon it emerge phase-coherent in the paraboloid aperture-plane, the effect of the flat annular plate, situated in the focal-plane,* is frequency dependent. The influence of the flat plate can once again be seen by noting the effect on phase and amplitude of the backscattered fields of Figure 21 between the innermost geometric bounds of the flat plate. A comparison between Figure 7 and Figure 21, as well as between Figure 11 and Figure 22, shows the variations introduced by interpolation of the subsystem data. The principal features are very similar although details are seen to vary in the far-field patterns.

Finally the <u>parabolic locus</u> was employed, <u>without</u> subsystem data <u>interpolation</u>. <u>Figure 23 and Figure 24</u> present the computed subsystem and far-field patterns, respectively. Satellite data were not available for comparison. This pattern, which represents the culmination of the entire effort, exhibits a first sidelobe level of -20 db at $\theta = 0.115$ degree, obliteration or filling of the second null, and a second sidelobe level of -28 db at $\theta = 0.230$ degree. The pattern at 15.3 GHz is characterized by features very similar to those at 7.3 GHz, where the first and second sidelobe levels were -20 db and -27 db, and where the second null was also obliterated. Since measured data of high quality were not available at 15.3 GHz it is necessary to appeal to the comparison between measured and computed results at 7.3 GHz and rely entirely on computed or simulated results at the higher frequency.

This would not be true if the plate were midway between the feed point F and the focus F of the paraboloid as this would constitute a degenerate pair of coincident hyperboloids.

Figure 1. NRL Microwave Space Research Facility (Waldorf, Md.)

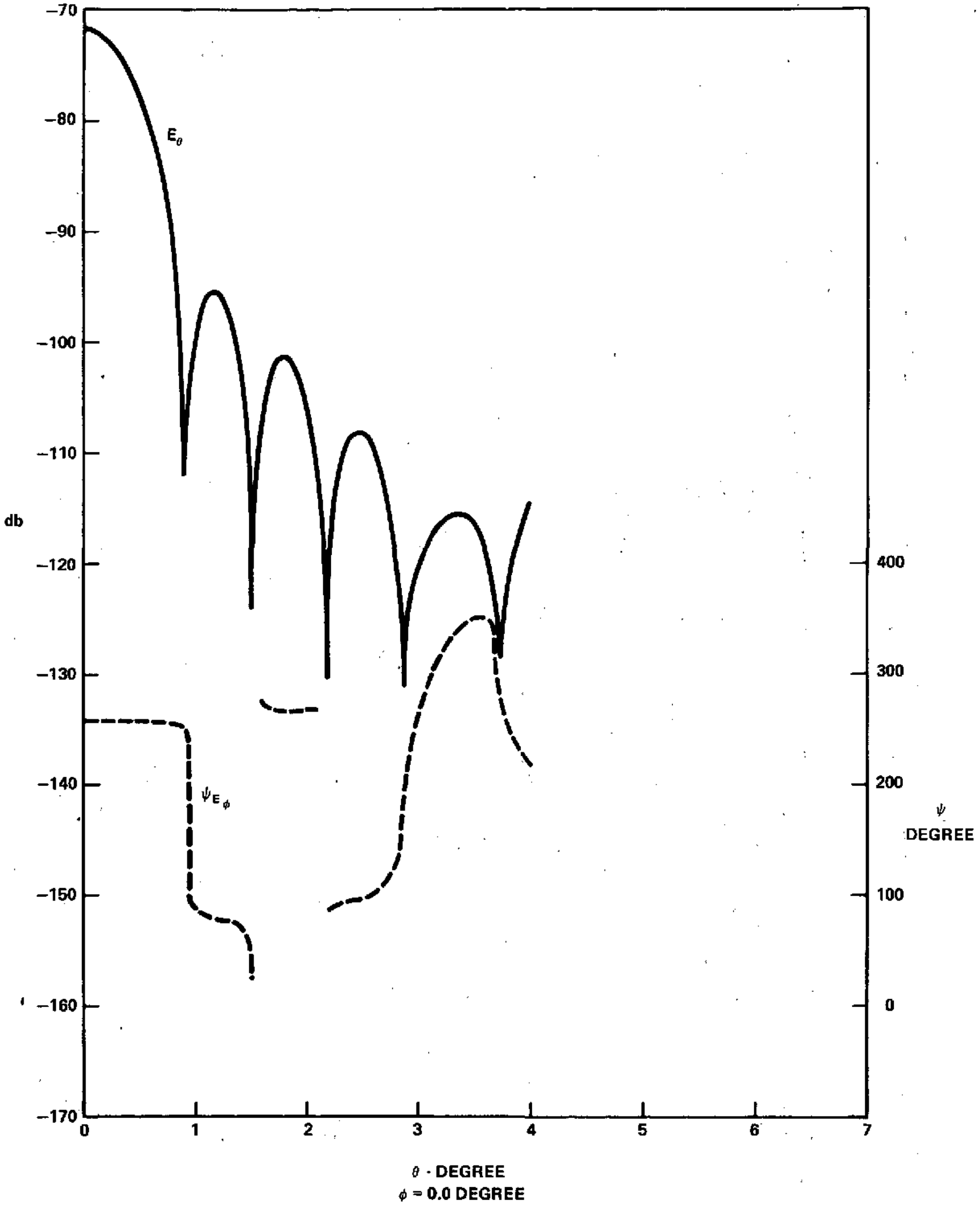

Figure 2. Far-field Radiation Pattern (f = 1.53 GHz)

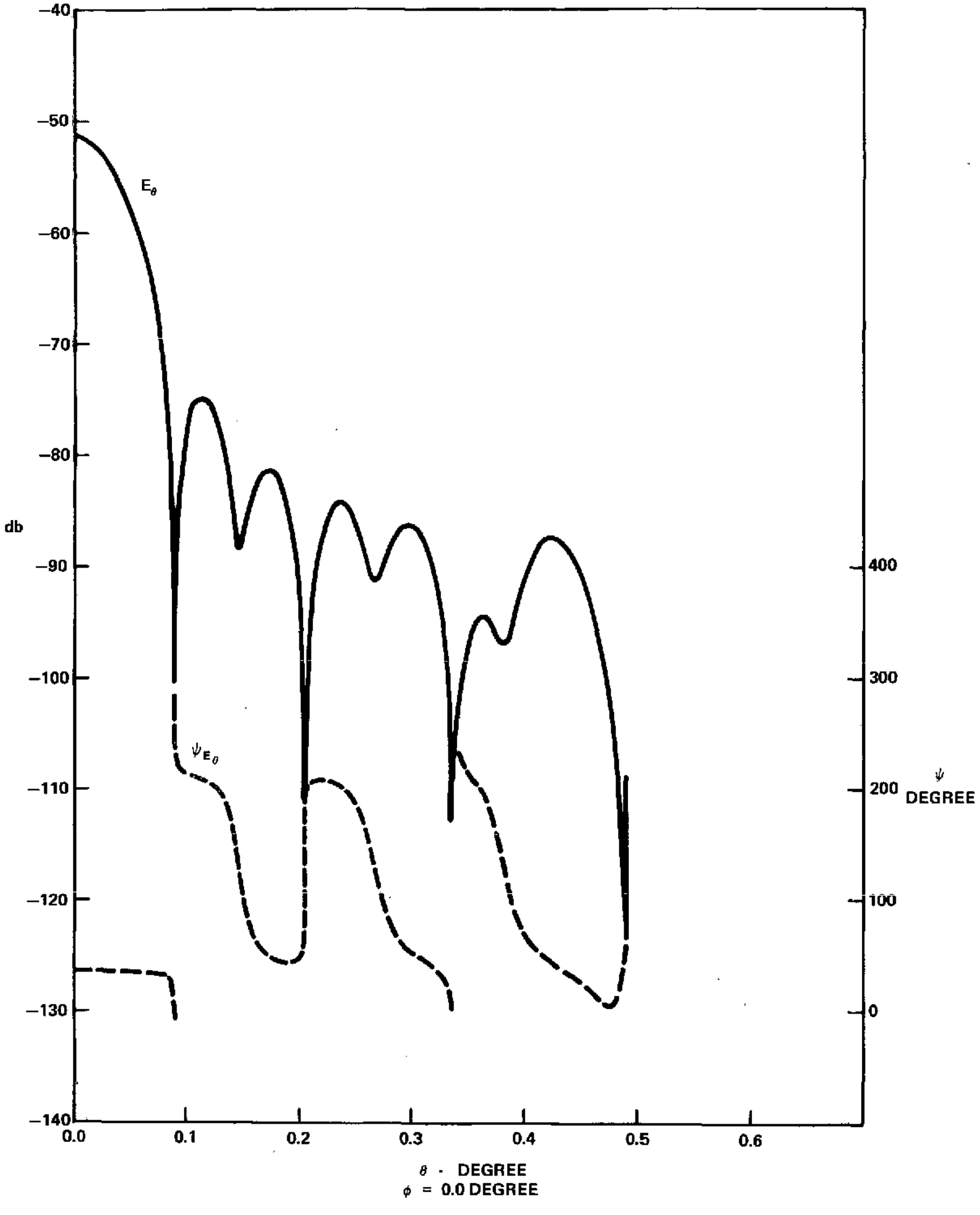

Figure 3. Far-field Radiation Pattern (f = 15.3 GHz)

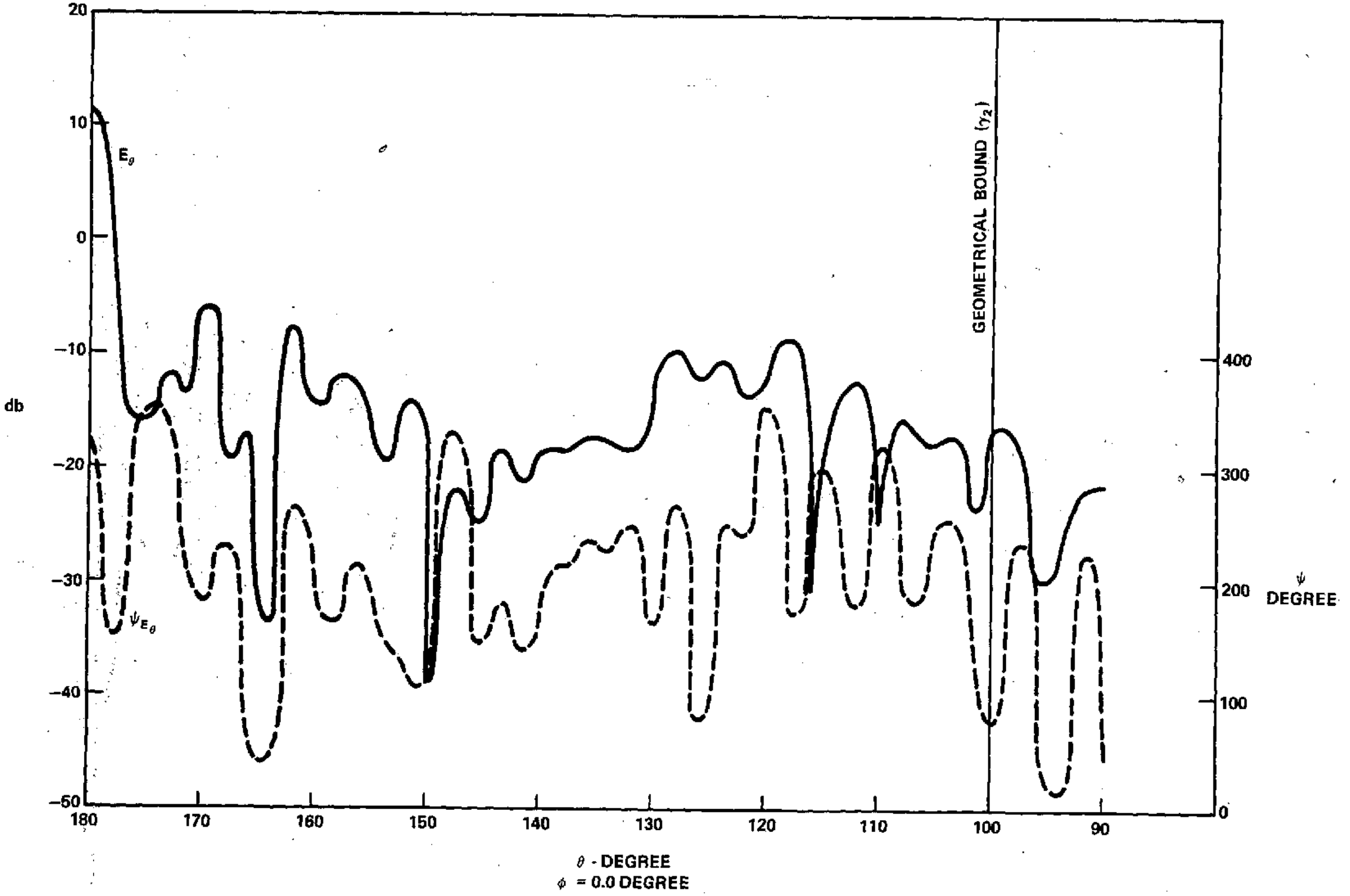

Figure 4. Hyperboloid Radiation Pattern at R = F (LI_1 = 1.25)

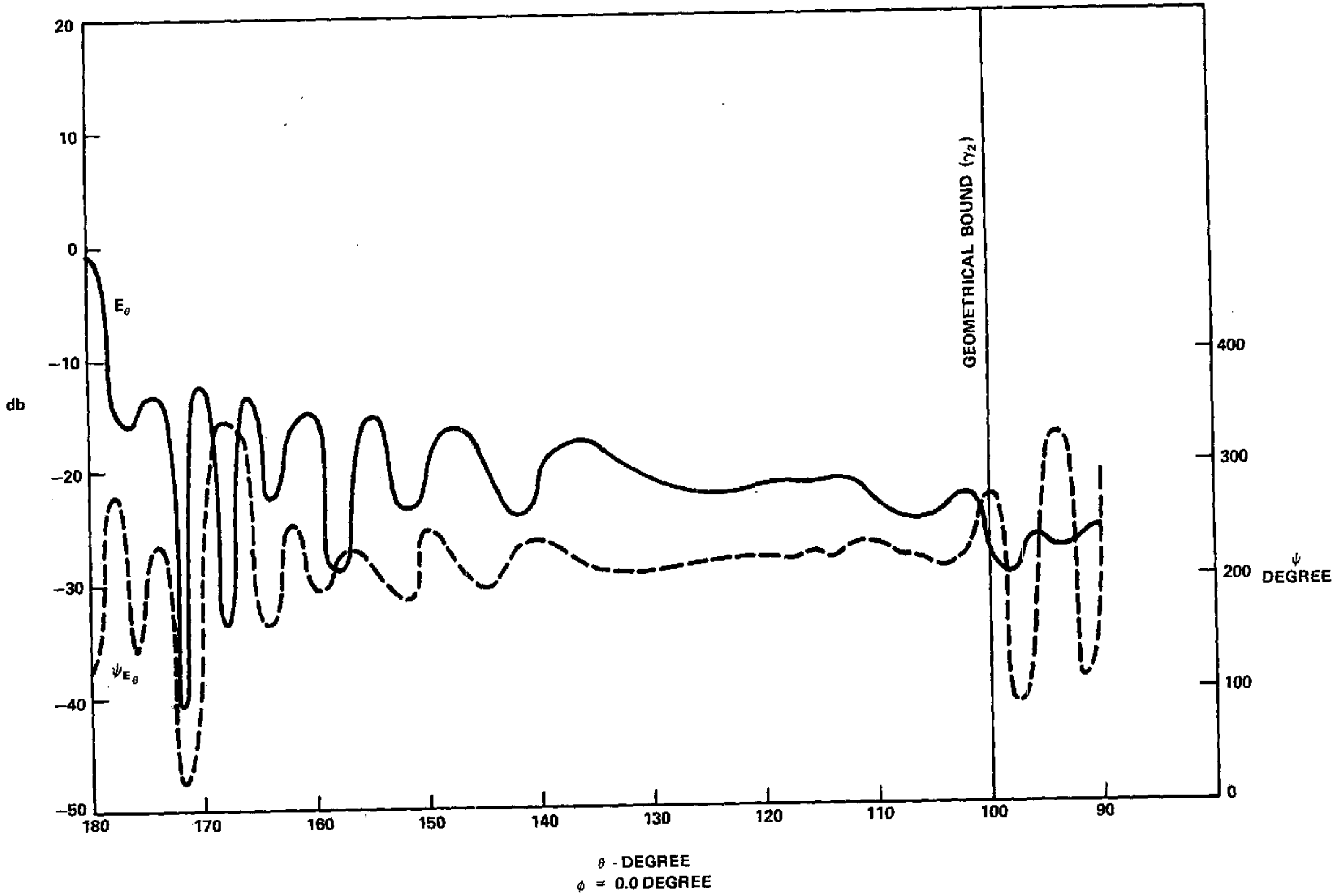
20
10
0
−10
−20
−30
−40
−50
db
E_θ
ψ_{E_θ}
GEOMETRICAL BOUND (γ_2)
400
300
200
100
0
ψ
DEGREE
180
170
160
150
140
130
120
110
100
90
θ - DEGREE
ϕ = 0.0 DEGREE

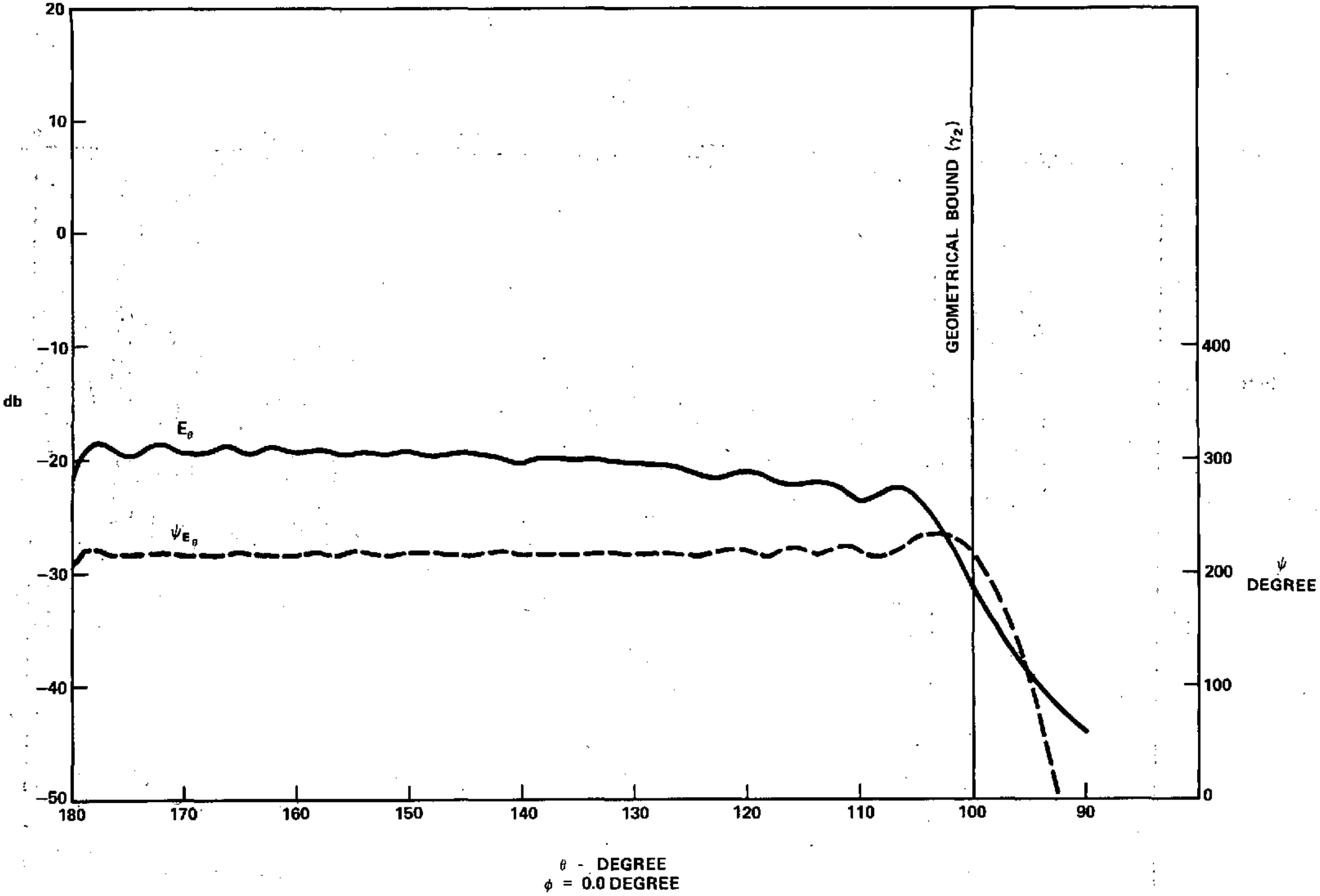

Figure 6. Hyperboloid Radiation Pattern at R = F (LI_1 = 0.300)

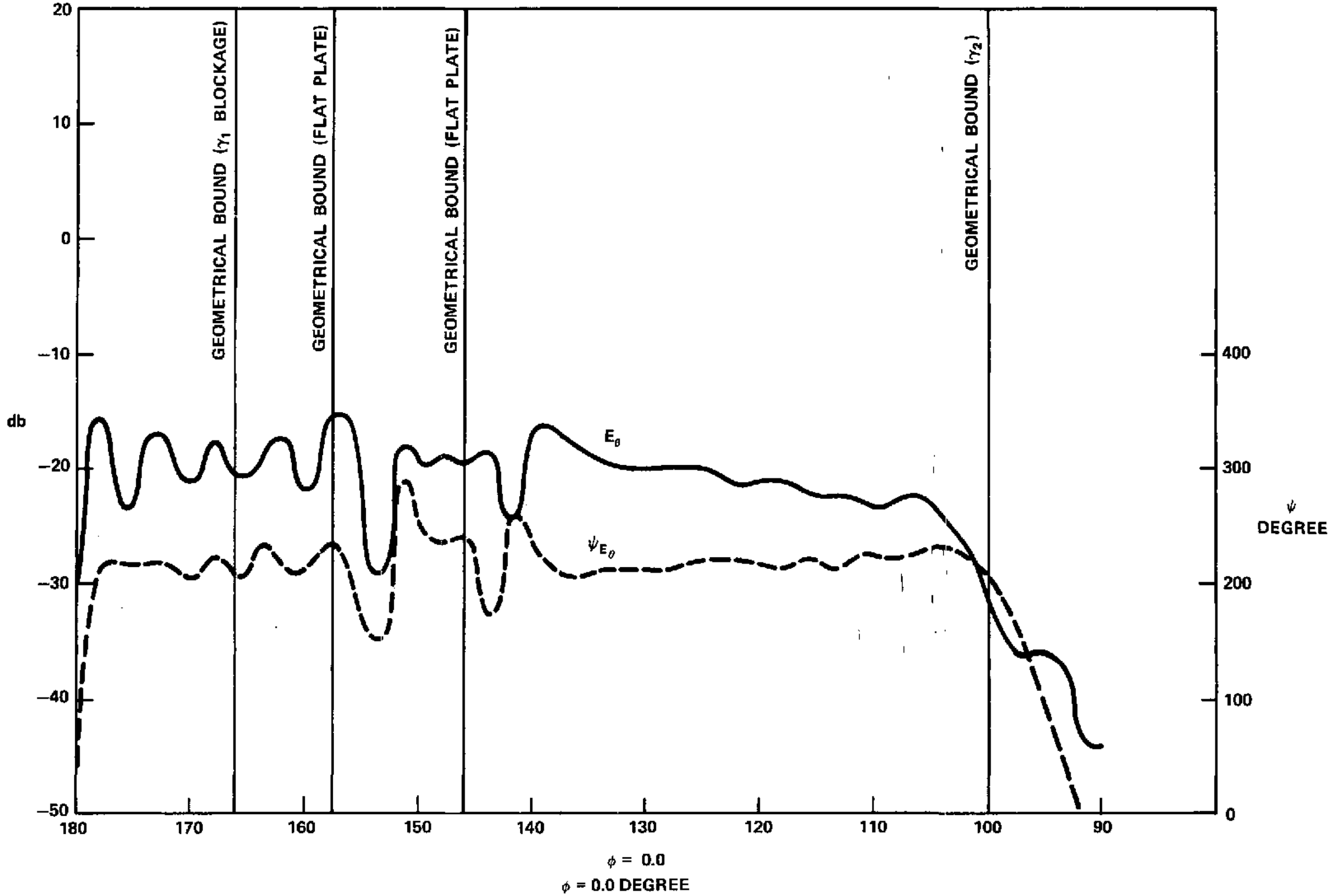

Figure 7. Hyperboloid-plate Radiation Pattern at R = F (LI_1 = 0.300, LI_1' = 1.00)

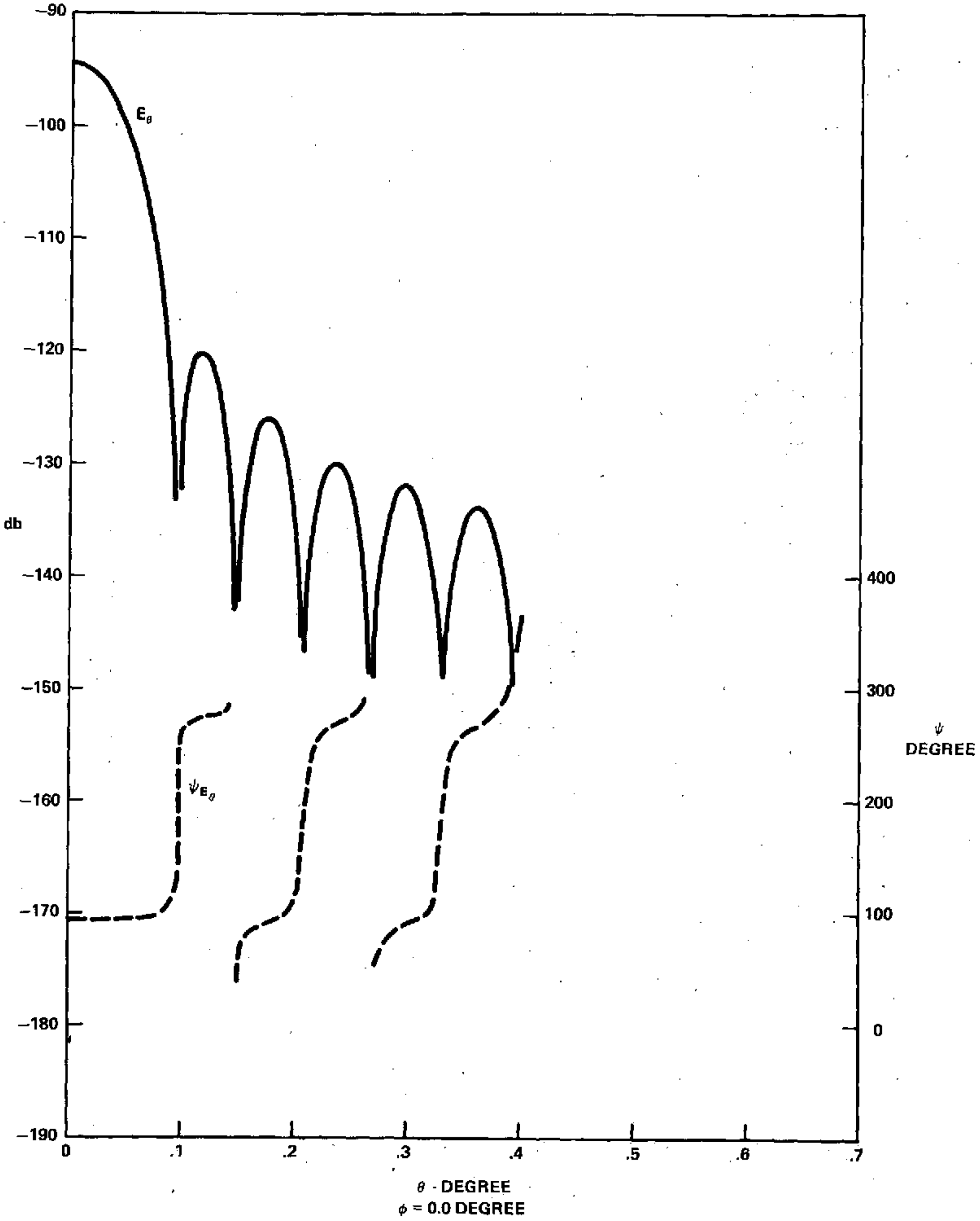

Figure 8. Far-field Reference Pattern

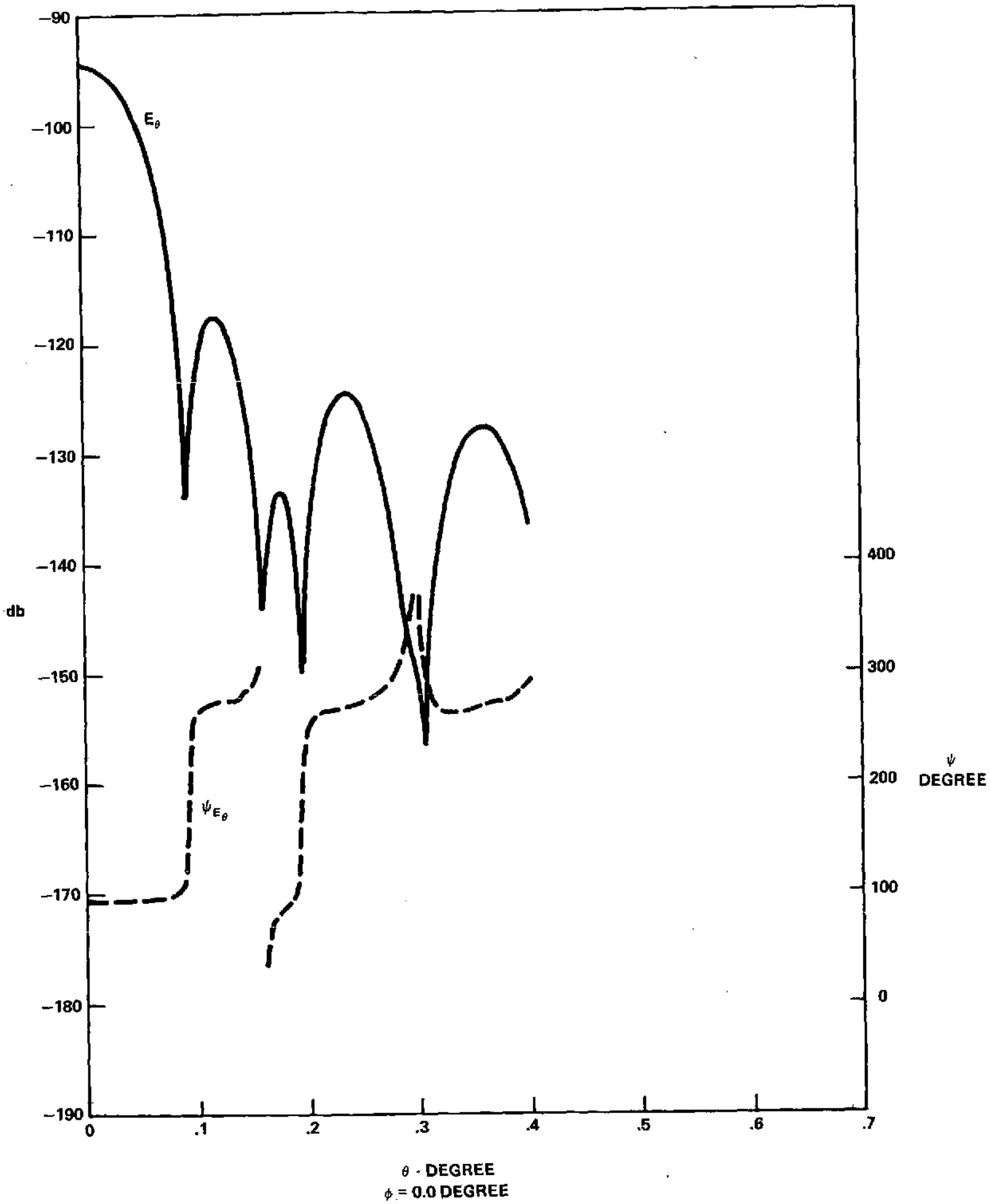

Figure 9. Far-field Pattern Showing Hyperboloid Blockage Effect

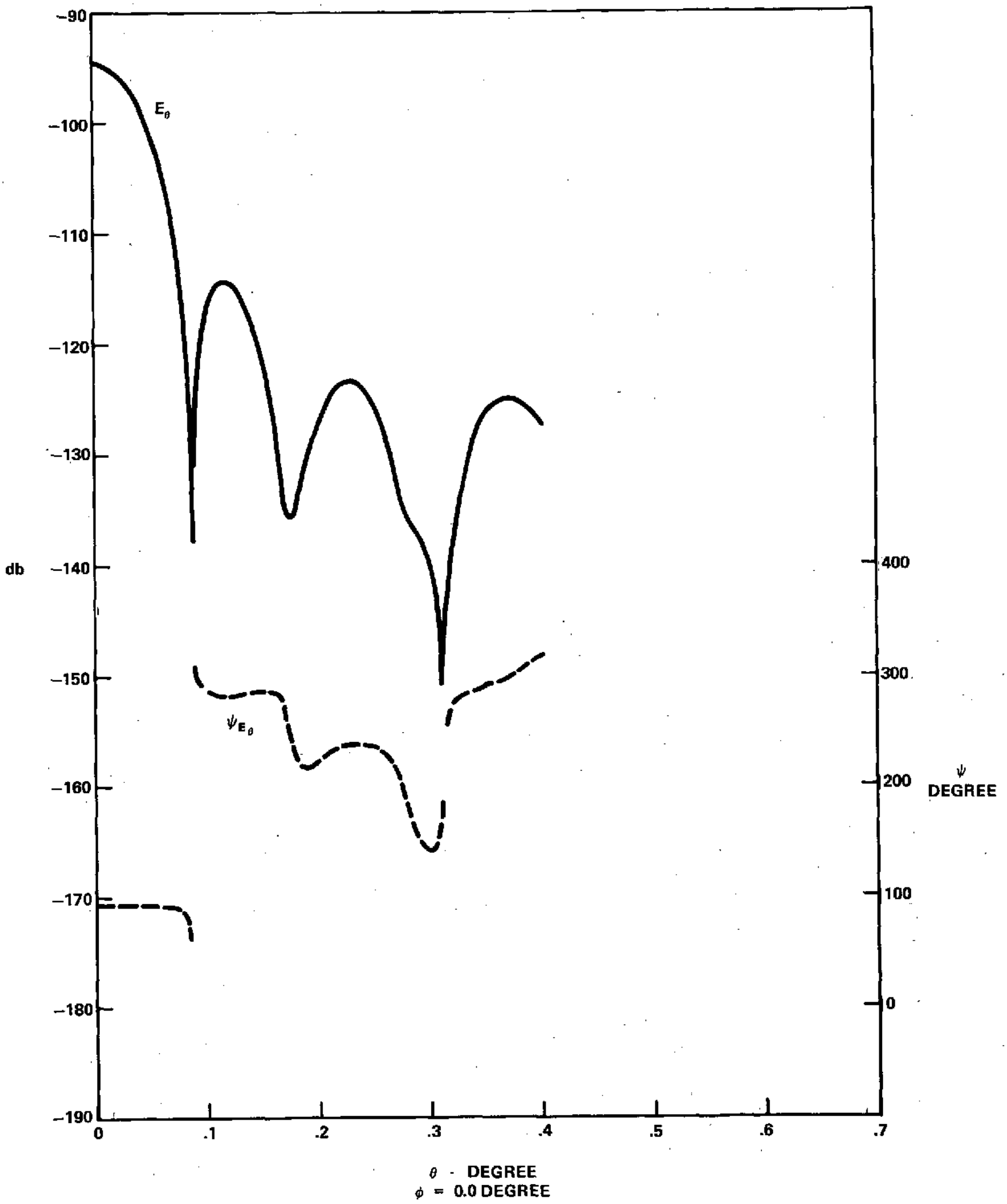

Figure 10. Far-field Pattern Showing Hyperboloid-plate Diffraction and Blockage Effects

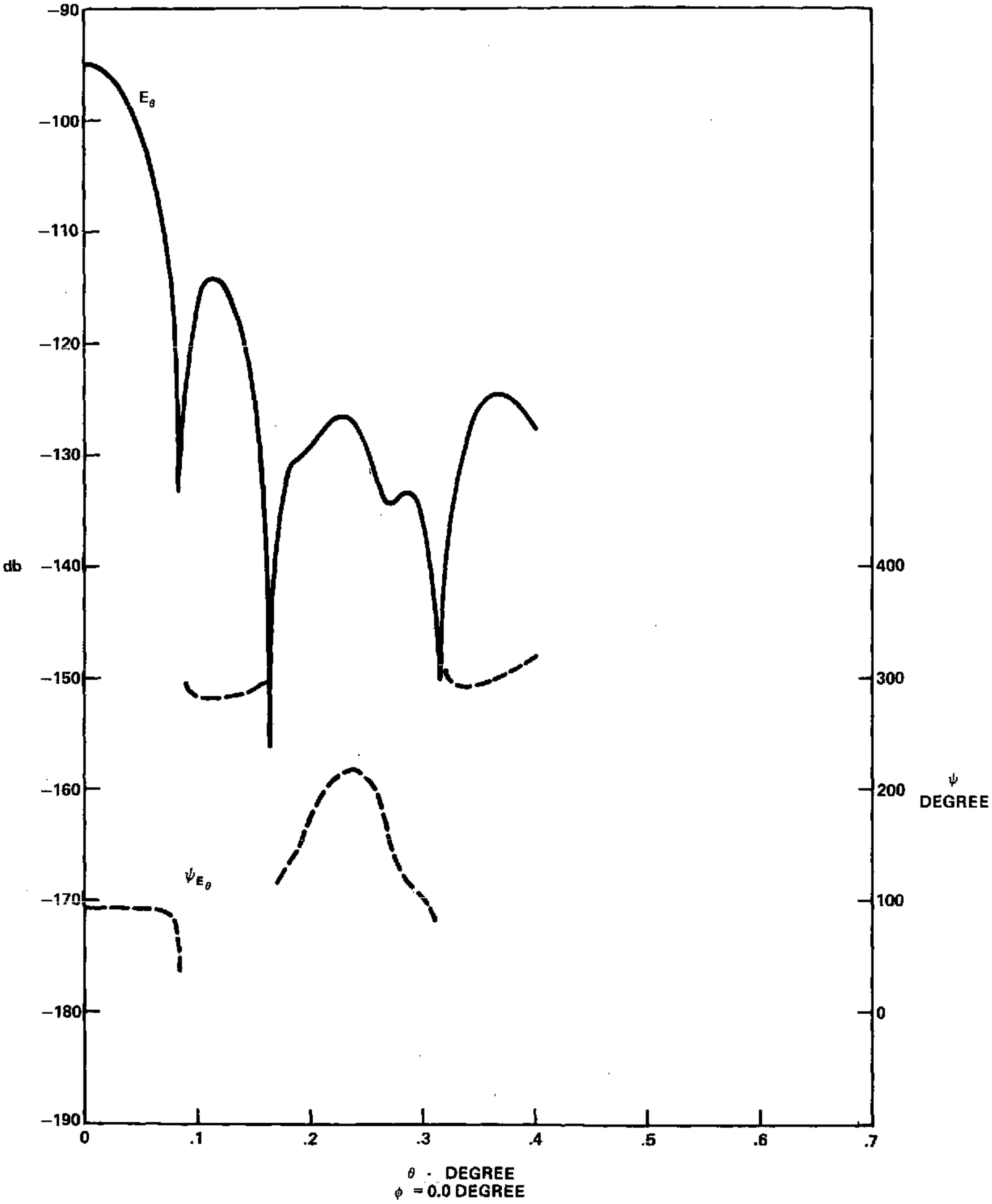

Figure 11. Far-field Pattern Showing Hyperboloid-plate Diffraction and Blockage Plus Truss-blockage Effects

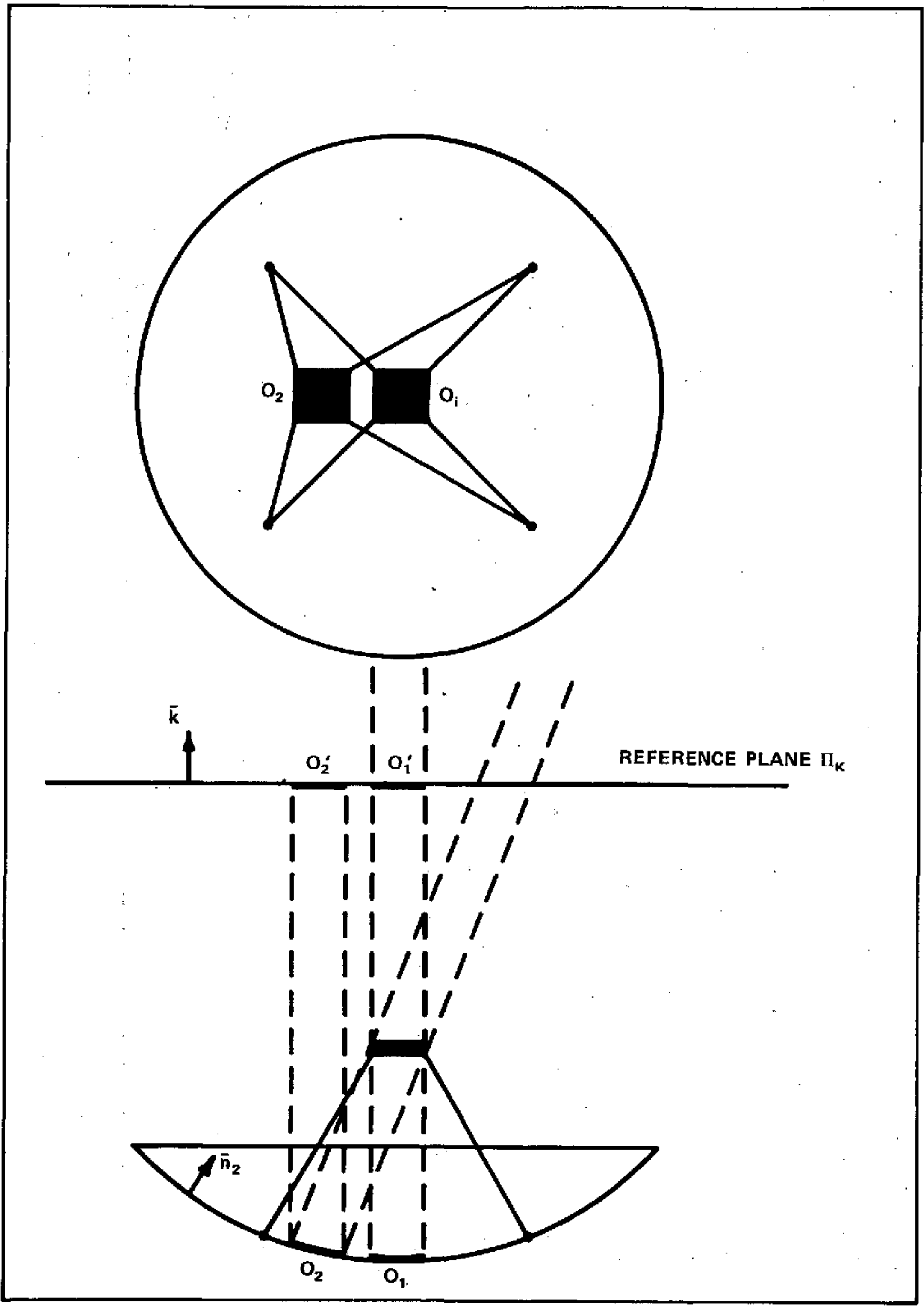

Figure 12. Secondary Blockage

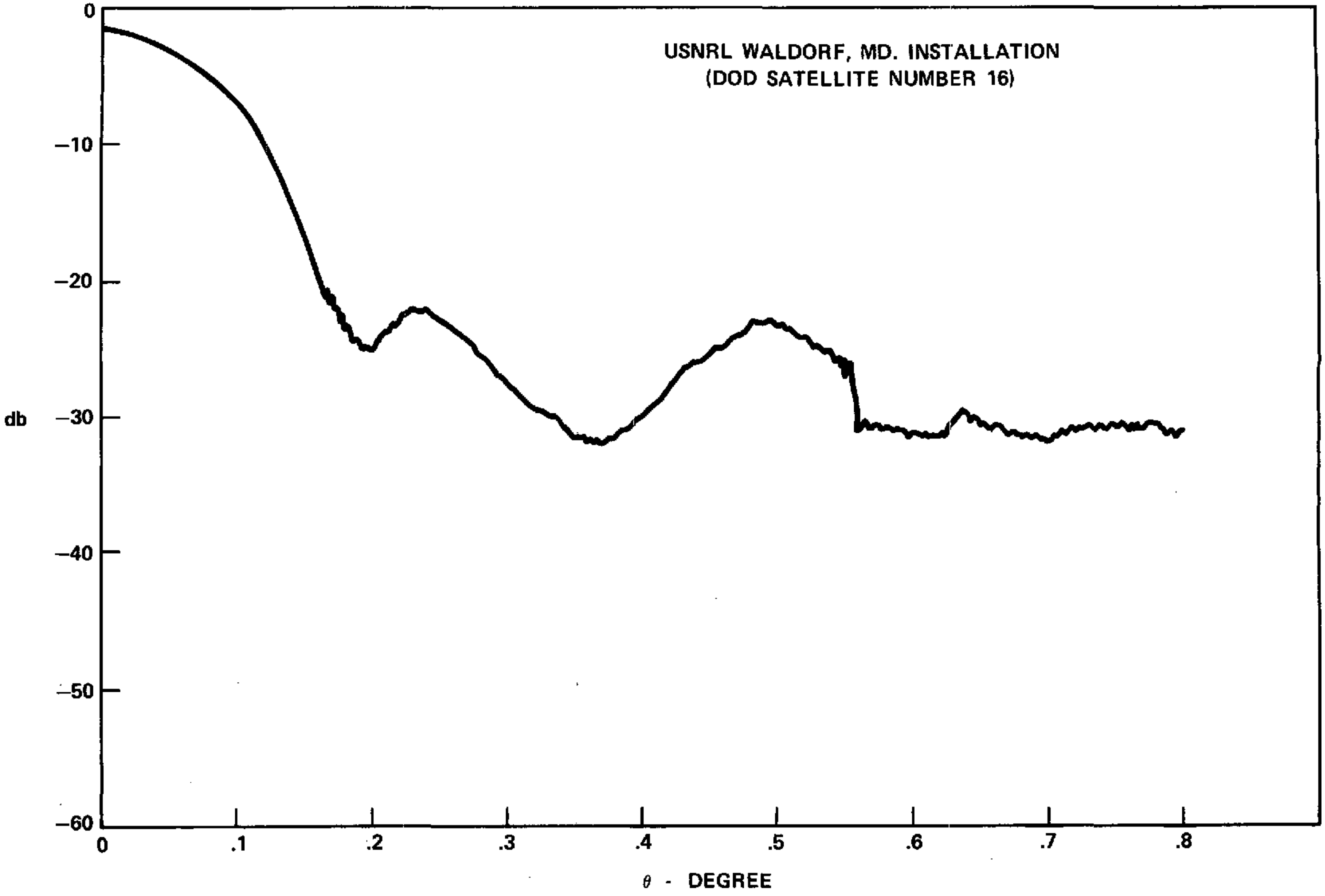

Figure 13. 7.3 GHz Radiation Pattern (Measured)

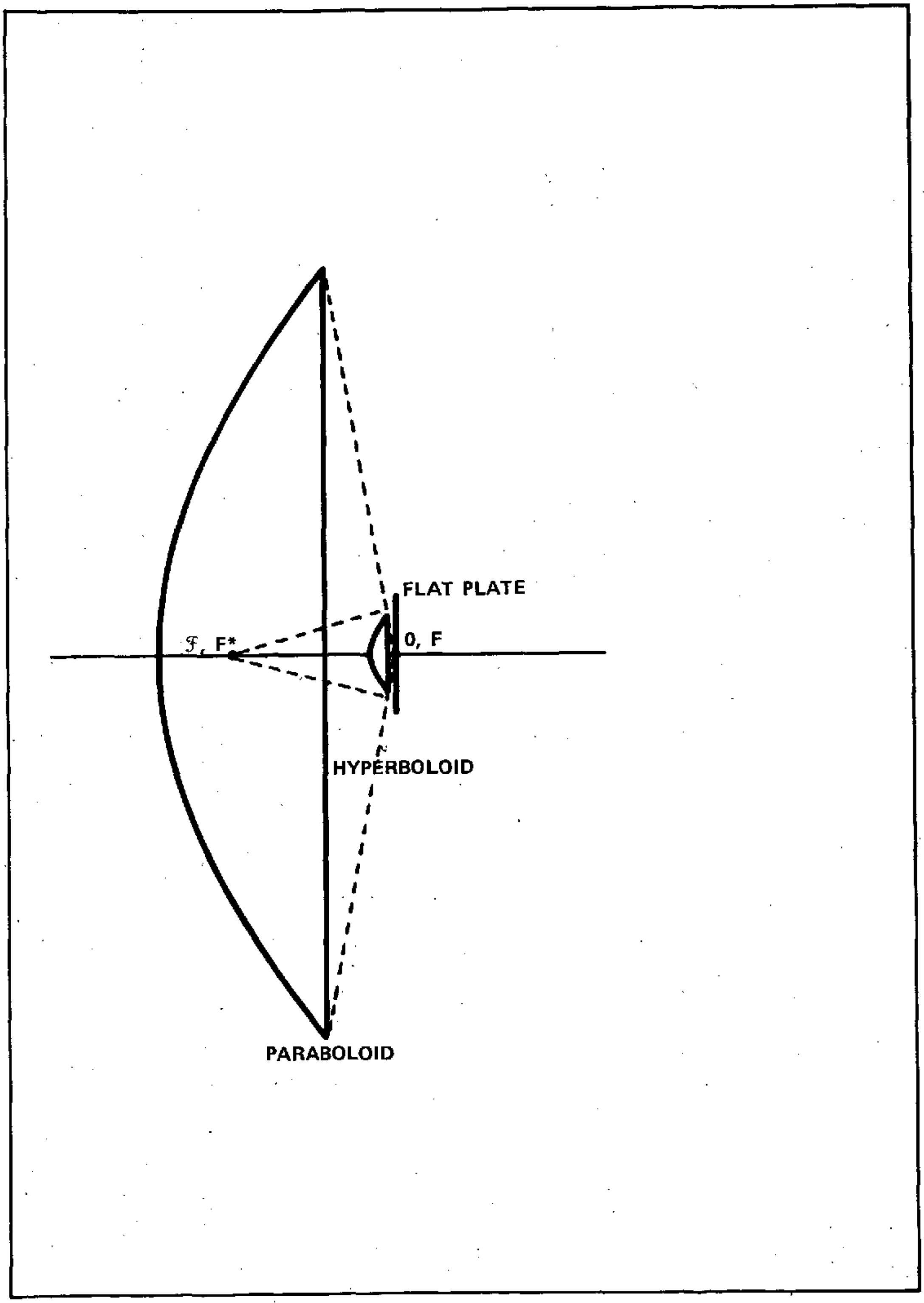

Figure 14. Reflector-System Geometry

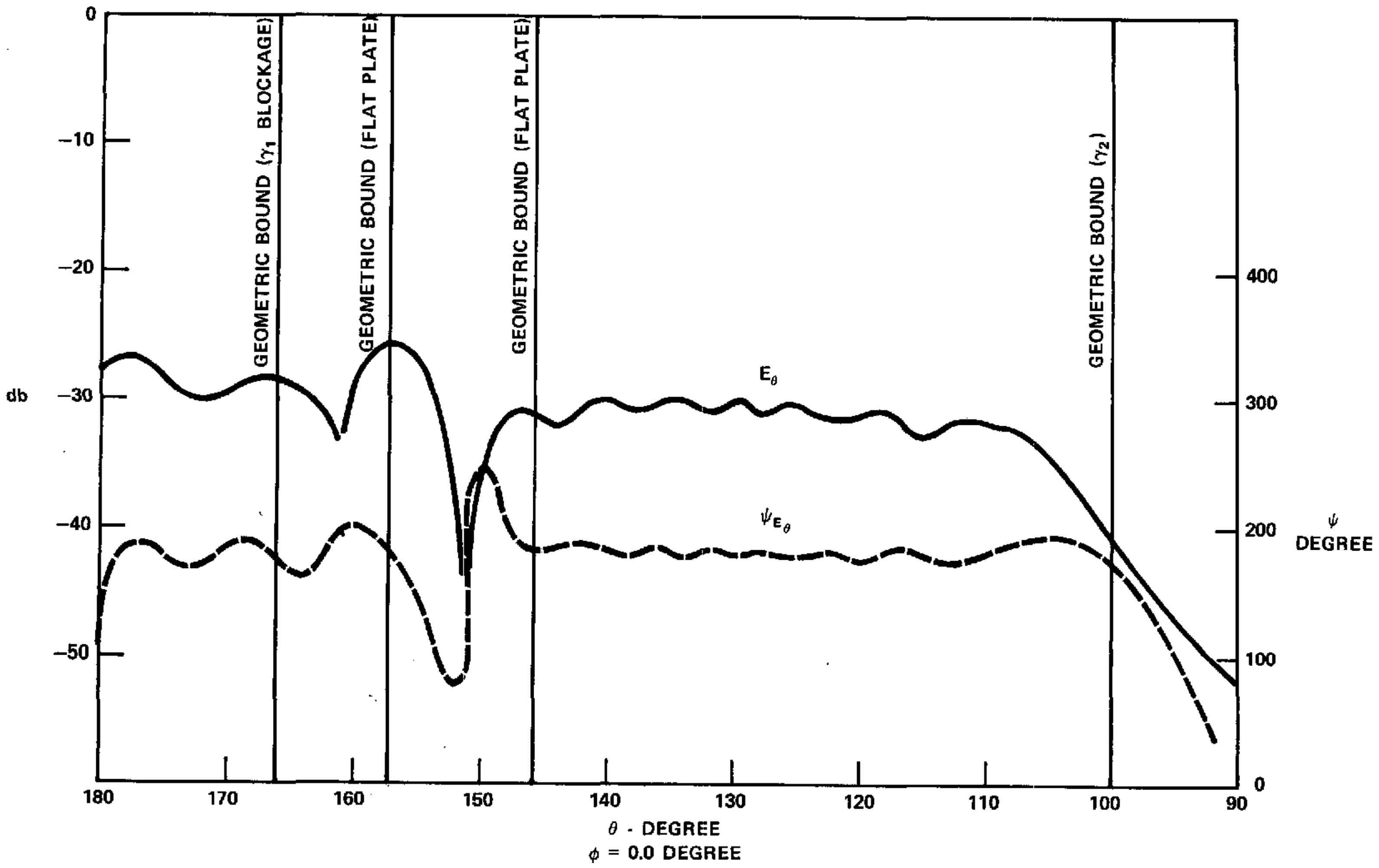

Figure 15. Hyperboloid-plate Radiation Pattern at R = F (LI_1 = 0.3) Using Interpolation

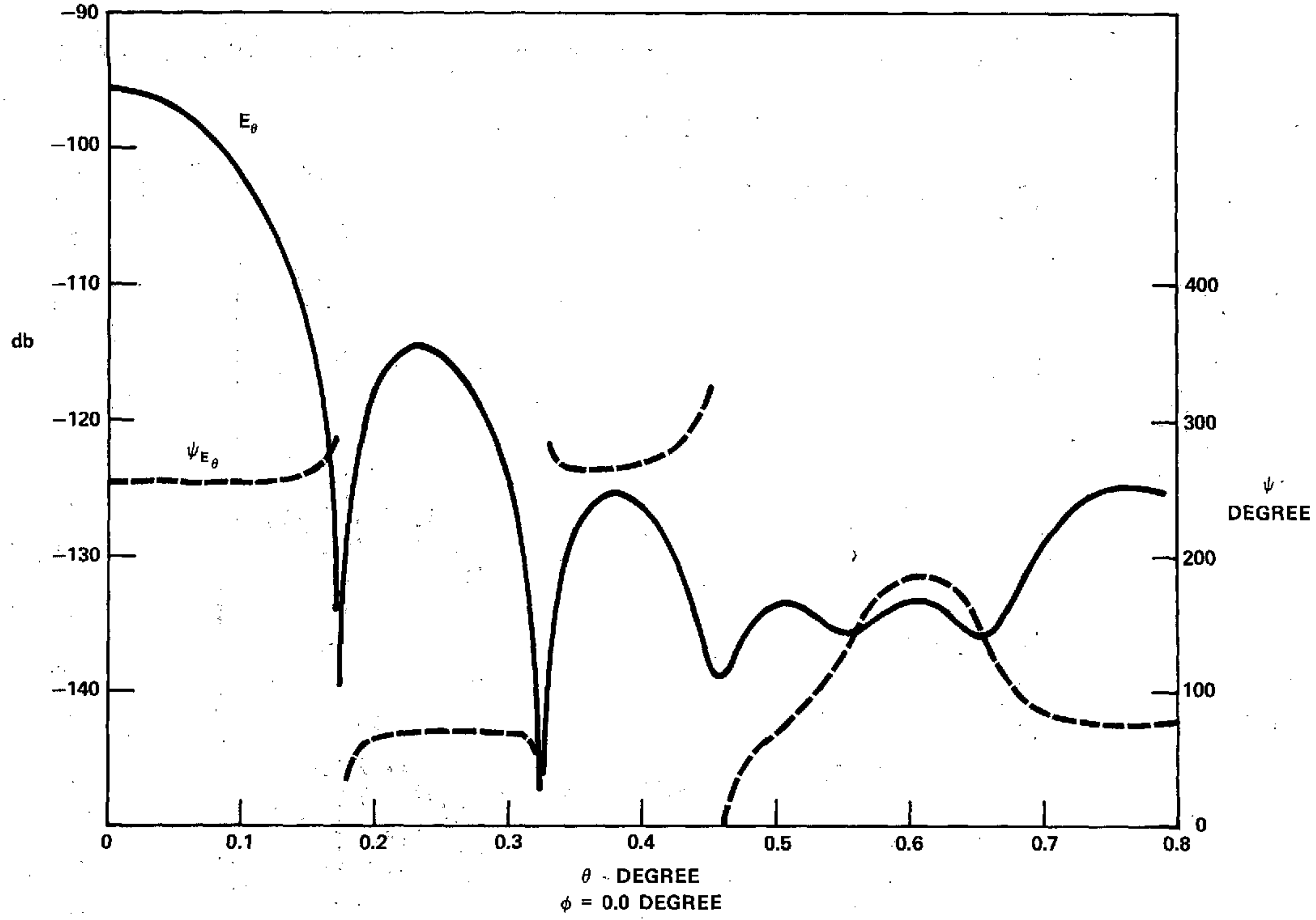

Figure 16. Far-Field Pattern (f = 7.3 GHz)

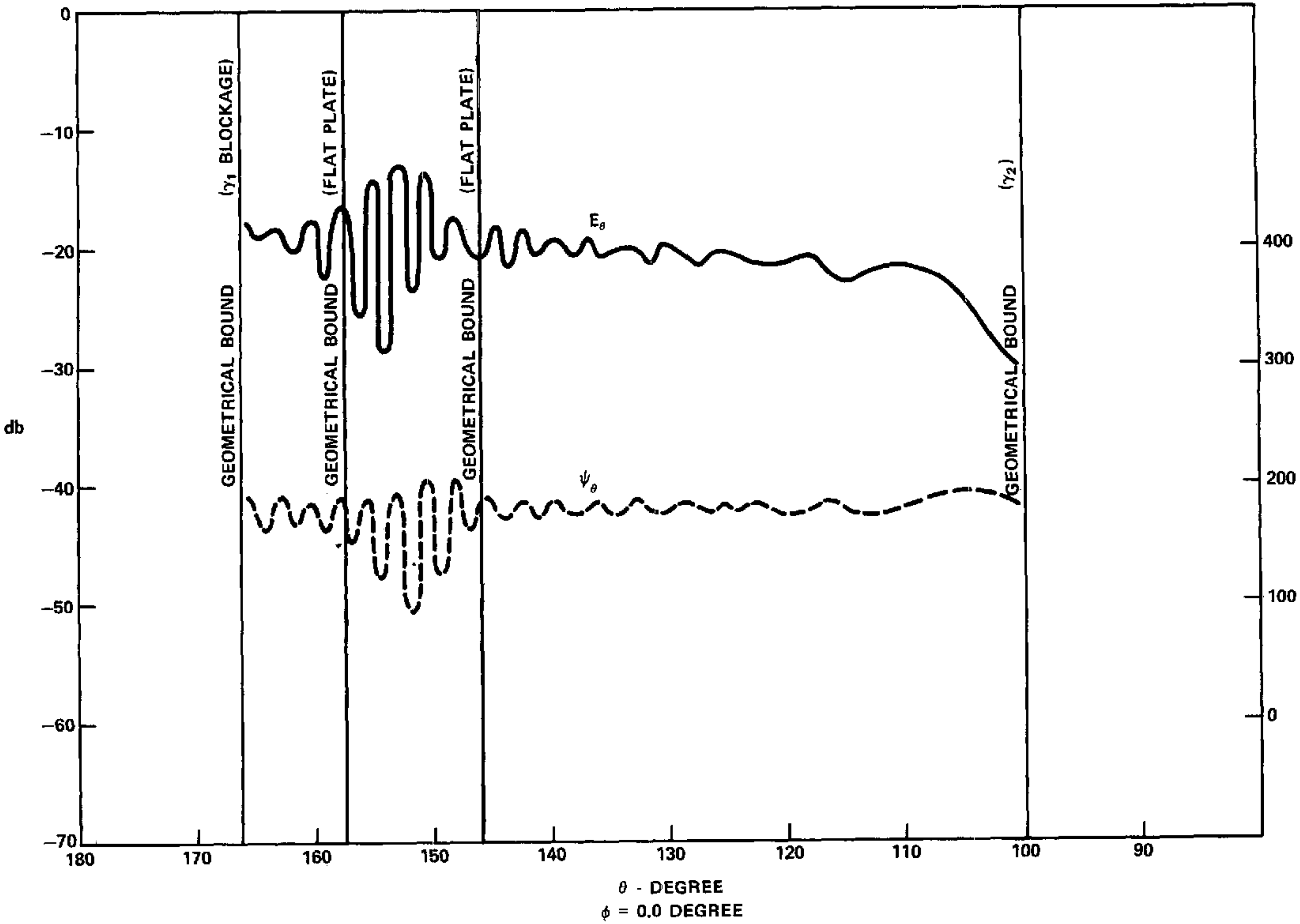

Figure 17. Hyperboloid-plate Radiation Pattern at R = F (LI_1 = 0.3) Without Interpolation

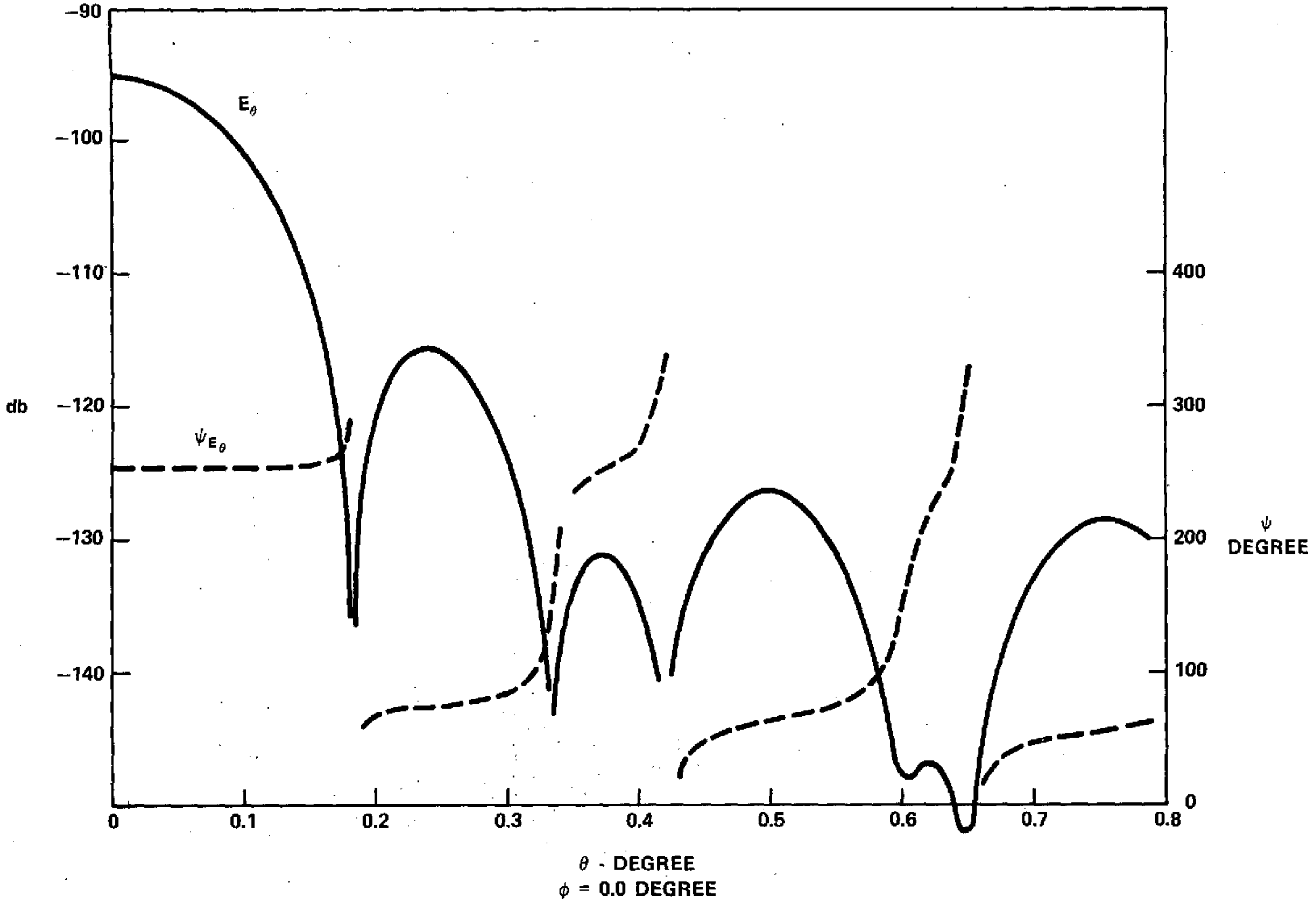

Figure 18. Far-field Pattern (f = 7.3 GHz)

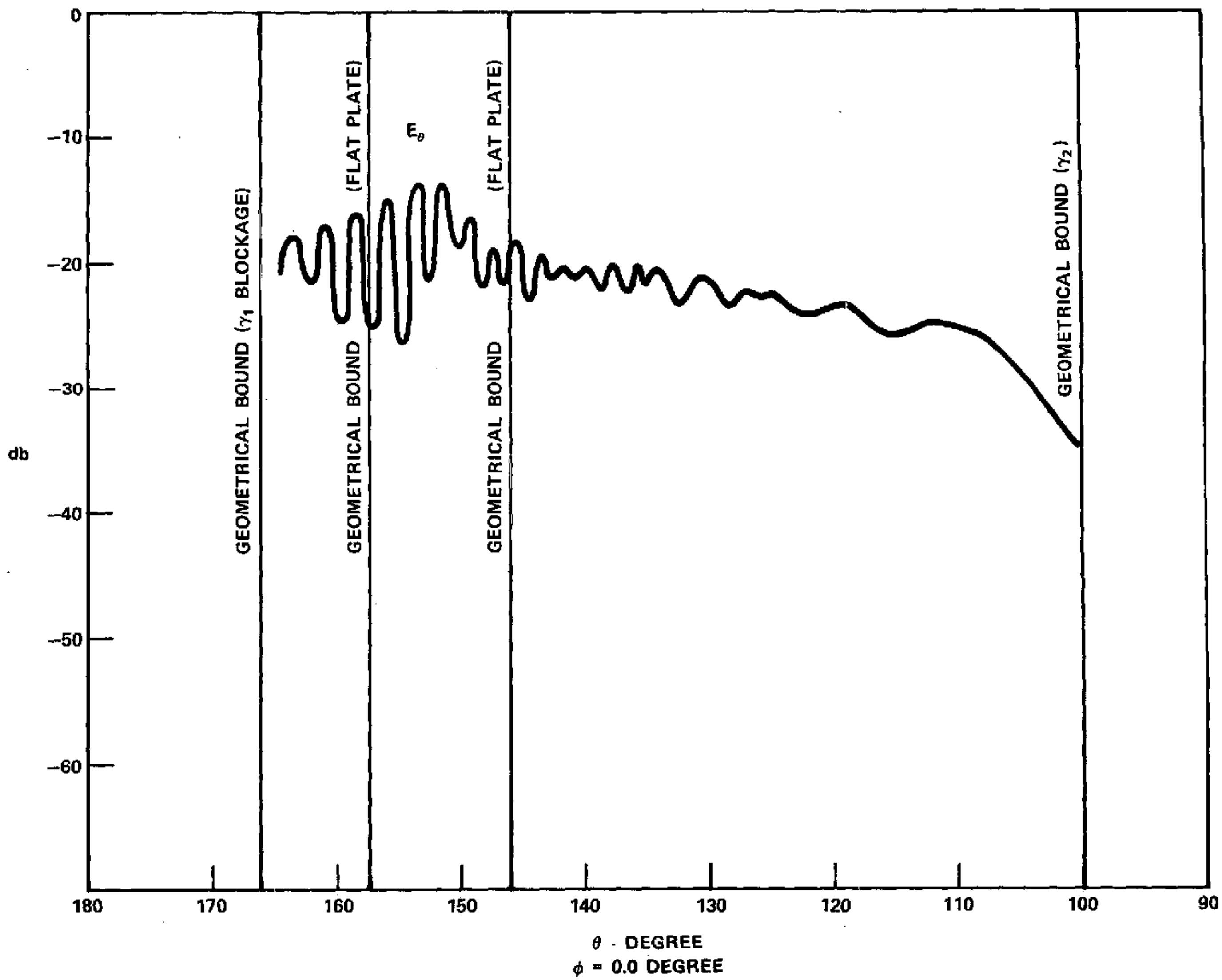

Figure 19. Hyperboloid-plate Radiation Pattern Without Interpolation on Parabolic Locus ($LI_1 = 0.3$)

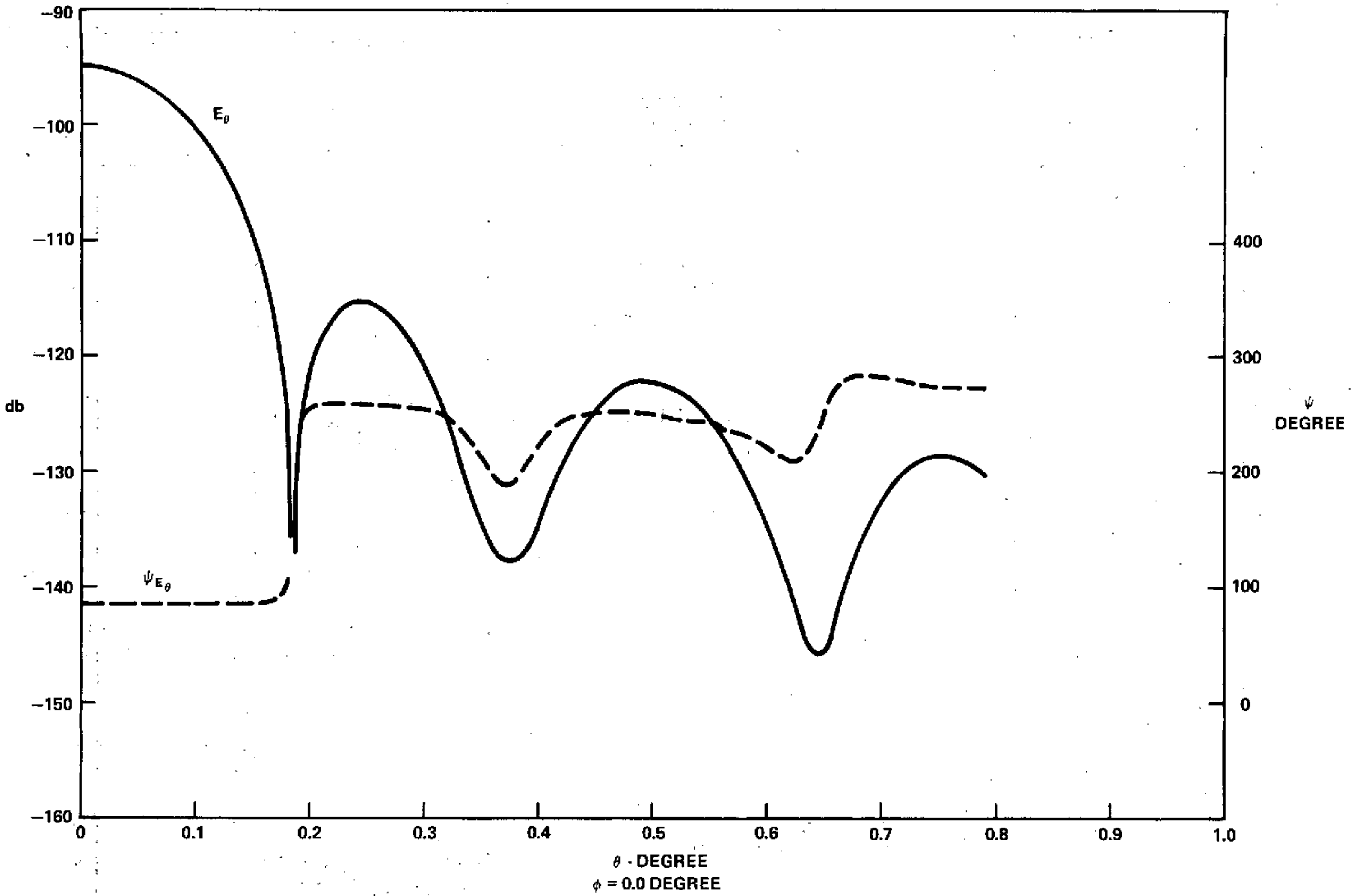

Figure 20. Far-field Pattern (f = 7.3 GHz)

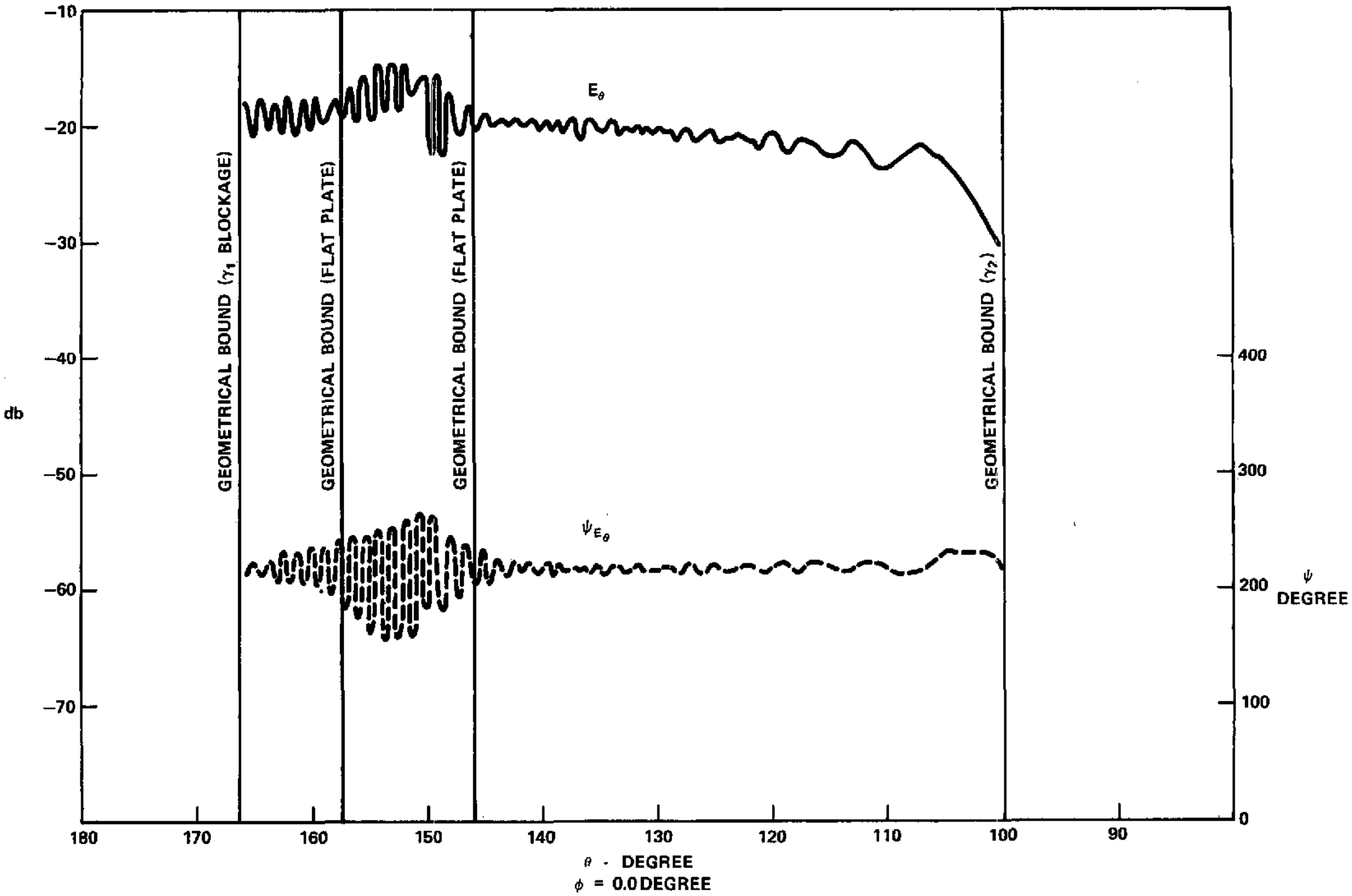

Figure 21. Hyperboloid-plate Radiation Pattern at R = F (LI_1 = 0.30) Without Interpolation

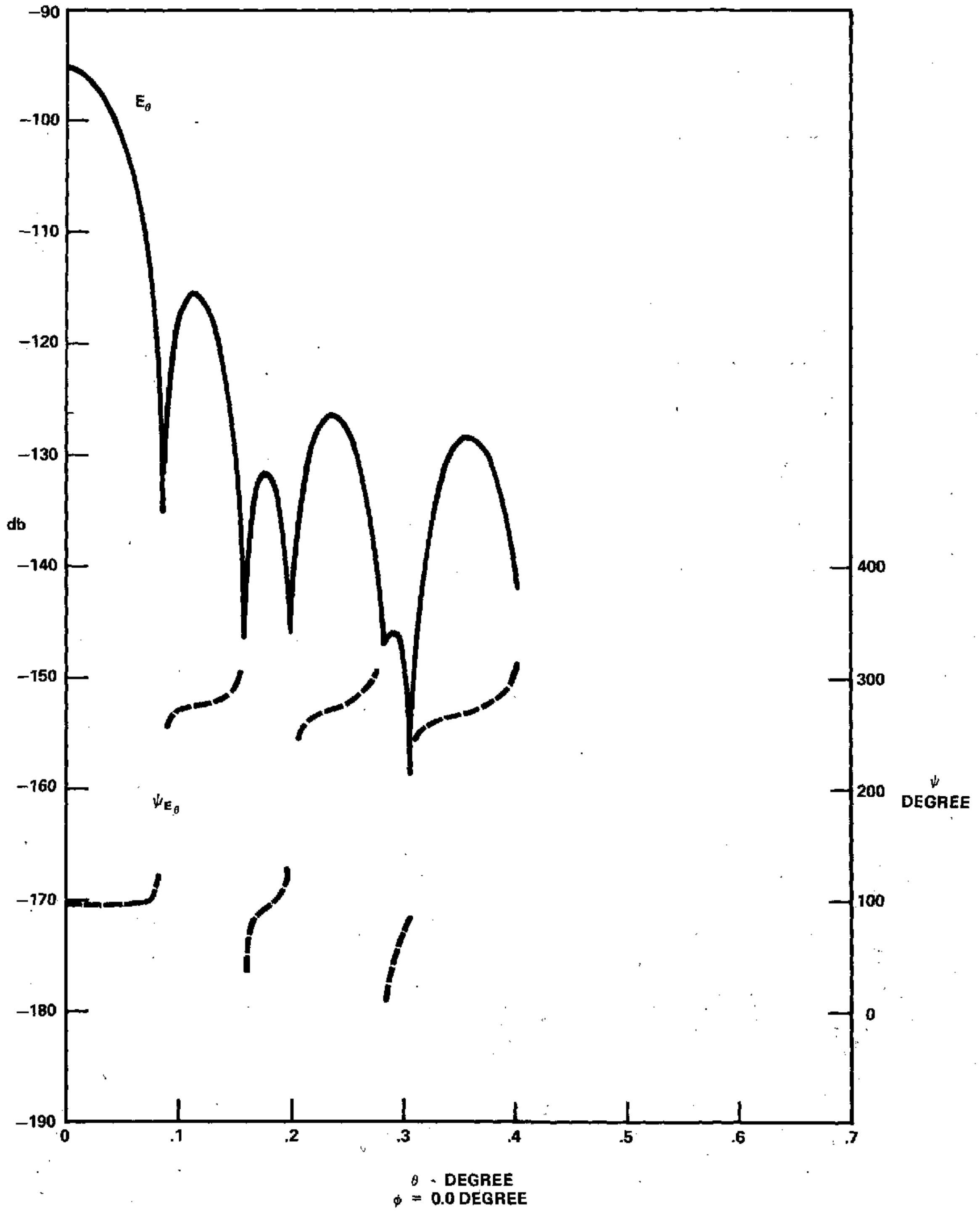

Figure 22. Far-field Pattern (f = 15.3 GHz)

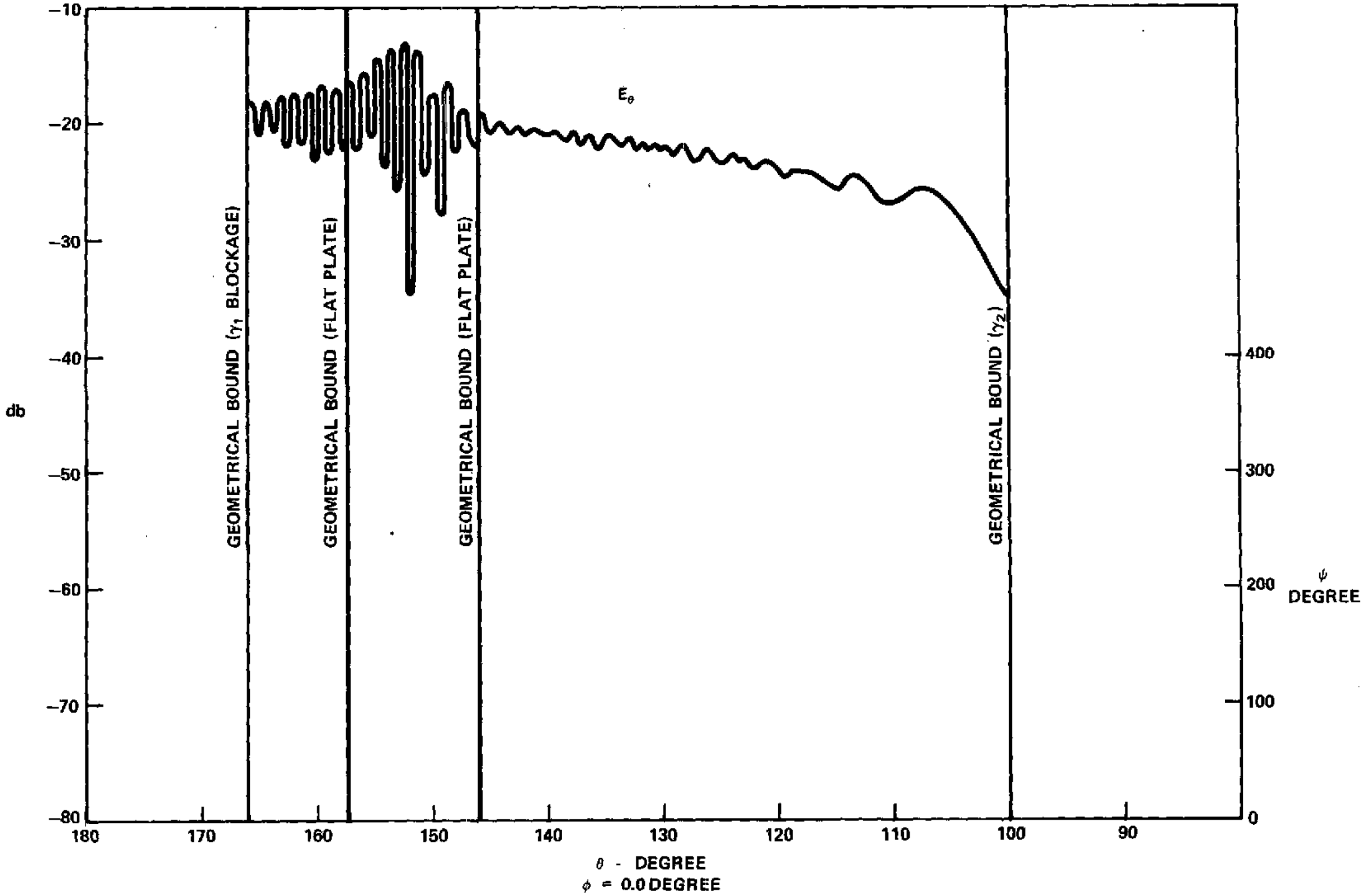

Figure 23. Hyperboloid-plate Radiation Pattern Without Interpolation on Parabolic Locus (LI_1 = 0.3)

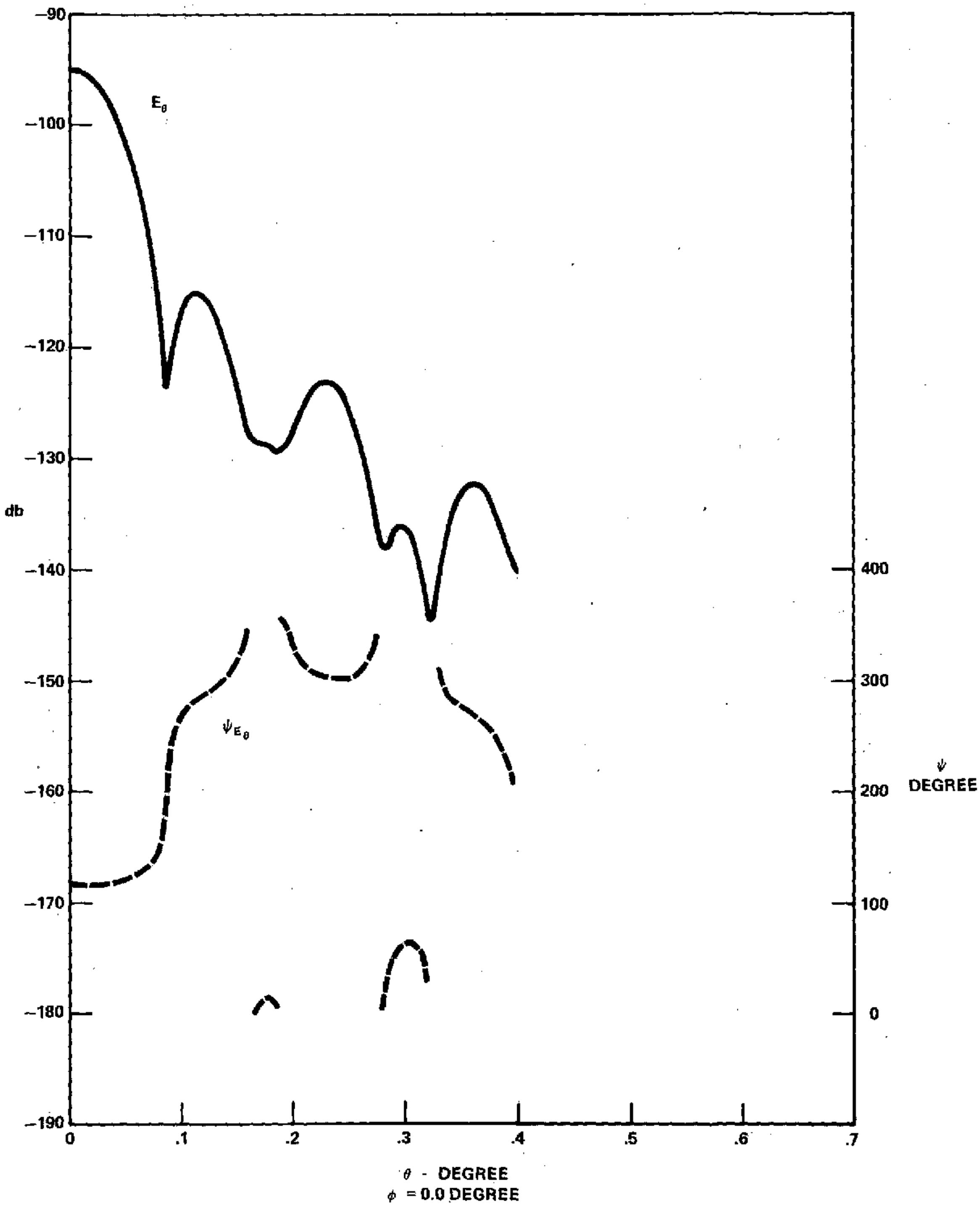

Figure 24. Far-field Pattern (f = 15.3 GHz)